HHS Public Access

Author manuscript

Nature. Author manuscript; available in PMC 2018 July 24.

Published in final edited form as:

Nature. 2018 February 01; 554(7690): 128–132. doi:10.1038/nature25460.

Mitochondrial translation requires folate-dependent tRNA methylation

Raphael J. Morscher[1,2], **Gregory S. Ducker**[1,2], **Sophia Hsin-Jung Li**[3], **Johannes A. Mayer**[4], **Zemer Gitai**[3], **Wolfgang Sperl**[4], and **Joshua D. Rabinowitz**[1,2]

[1]Lewis-Sigler Institute for Integrative Genomics, Princeton University, Princeton, NJ 08544, USA

[2]Department of Chemistry, Princeton University, Princeton, NJ 08544, USA

[3]Department of Molecular Biology, Princeton University, Princeton, NJ 08544, USA

[4]Department of Pediatrics, Salzburger Landeskliniken and Paracelsus Medical University, Salzburg, 5020, Austria

Abstract

Folates enable the activation and transfer of one-carbon units for biosynthesis of purines, thymidine and methionine[1–3]. Antifolates are important immunosuppressive[4] and anticancer agents[5]. In proliferating lymphocytes[6] and human cancers[7,8], folate enzymes localizing to the mitochondria are particularly strongly upregulated. This in part reflects the need for mitochondria to generate one-carbon units and export them to the cytosol for anabolic metabolism[2,9]. The full range of uses of folate-bound one-carbon units in the mitochondrial compartment itself, however, has not been thoroughly explored. Here we show that loss of catalytic activity of the mitochondrial folate enzyme serine hydroxymethyltransferase 2 (SHMT2), but not other folate enzymes, leads to defective oxidative phosphorylation due to impaired mitochondrial translation. We find that SHMT2, presumably by generating mitochondrial 5,10-methylenetetrahydrofolate, provides methyl donors for producing the taurinomethyluridine base at the wobble position of select mitochondrial tRNAs. Mitochondrial ribosome profiling reveals that SHMT2 knockout cells, due to lack of this modified base, suffer from defective translation with preferential mitochondrial ribosome stalling at certain lysine (AAG) and leucine (UUG) codons. This results in impaired respiratory chain enzyme expression. Stalling at these specific codons also occurs in certain mitochondrial inborn errors of metabolism. Disrupting whole-cell folate metabolism, by folate deficiency or antifolate therapy, also impairs the respiratory chain. In summary, mammalian

Correspondence to: Joshua D. Rabinowitz.

Author Contributions

R.J.M., G.S.D., and J.D.R. conceived of the project and designed the experiments. R.J.M. and J.D.R. wrote the manuscript. R.J.M., G.S.D. and S.H.L performed biochemical experiments. Z.G. and W.S. were involved in study design and data interpretation. W.S. and J.A.M. contributed primary patient cell lines. All authors reviewed and edited the manuscript before submission.

Competing financial interests

The authors declare no competing financial interests.

Data deposition

Raw sequencing data are available from Sequence Read Archive under BioProject accession number PRJNA419990.

mitochondria use folate-bound one-carbon units to methylate tRNA, and this modification is required for respiratory chain translation and thus oxidative phosphorylation.

The major source of folate one-carbon (1C) units in mammalian cells is the amino acid serine[1–3]. Transfer of serine's 1C unit to tetrahydrofolate (THF) can occur in either the cytosol or mitochondrion, via SHMT1 or SHMT2, respectively[10] (Figure 1a). Evidence from stable isotope tracing indicates that cancer cells predominantly use SHMT2 to catabolize serine, exporting the resulting 1C units to the cytosol to support nucleotide synthesis[2,9]. The extent to which 1C unit production via SHMT2 is also important to support mitochondrial health has yet to be determined.

In characterizing a set of human HCT116 colon cancer CRISPR deletion cell lines lacking folate 1C enzymes, we serendipitously discovered that loss of SHMT2 induces change in media color indicating enhanced extracellular acidification (Extended Data Fig. 1a). Quantitative analysis of media confirmed increased glucose uptake and lactate secretion. This effect was SHMT2 specific: loss of other core 1C enzymes, including other mitochondrial enzymes (MTHFD2 and MTHFD1L) and SHMT1, did not induce glycolysis (Figure 1b, Extended Data Fig. 1b).

A common cause of increased glycolytic flux is respiratory deficiency[11]. Loss of SHMT2 reduced both basal respiration and maximal respiratory capacity and decreased the NAD^+/NADH ratio in multiple HCT116 (Figure 1c, Extended Data Fig. 1c) and HEK293T SHMT2 knockout clones, but not knockouts of other core folate 1C enzymes (Extended Data Fig. 1d, e). Consistent with respiratory chain deficiency, SHMT2 loss decreased glucose flux into the TCA cycle intermediate citrate, with an increased fraction of citrate instead being produced by reductive carboxylation[12]. As reported recently in other models of mitochondrial damage[13,14], pool size of TCA cycle metabolites and associated amino acids was also decreased (Extended Data Fig. 1f, g). To identify the cause of respiratory deficiency, we examined the abundances of several mitochondrial proteins, finding decreased abundance of complex I, IV, and V subunits with retained levels of complex II, III and markers of mitochondrial mass (Figure 1d and Extended Data Fig. 1h, i). Thus, SHMT2 is required to maintain levels of multiple mitochondrial respiratory chain proteins.

Given that loss of SHMT2, but not the immediate downstream enzymes of mitochondrial 1C metabolism, caused impaired oxidative phosphorylation, we were curious if the phenotype reflected a requirement for SHMT2's catalytic activity, or alternatively a non-catalytic role of SHMT2, perhaps related to its reported interaction with the mitochondrial nucleoid[15]. Accordingly, in the SHMT2 knockout background, we stably re-expressed catalytic inactive SHMT2 (p.Glu98Leu/p.Tyr106Phe), PLP-binding mutant SHMT2 (p.Lys280Gln) or wild-type SHMT2 protein (Extended Data Fig. 2 and 3a). Re-expression of wild-type protein, but not the catalytically inactive mutants, rescued oxidative phosphorylation deficiency (Figure 1e, Extended Data Fig. 3b) and normalized glycolytic flux (Extended Data Fig. 3c). In addition, SHMT2 re-expression rescued the growth defect of SHMT2 knockout cells[9] (Extended Data Fig. 3d) and normalized 1C metabolism (Extended Data Fig. 3e, f). Thus, mitochondrial SHMT catalytic activity is critical to sustain oxidative phosphorylation.

Two compartment-specific uses of mitochondrial folate 1C units have been reported: the local biosynthesis of deoxythymidine triphosphate (dTTP)[16,17] and of formyl-methionine (f-Met)[18,19] (Figure 2a). Production of dTTP requires 5,10-methylene-THF (methylene-THF), whereas f-Met requires 10-formyl-THF (formyl-THF). SHMT2 is upstream of both compounds, and thus SHMT2 loss would be expected to deplete both. In contrast, MTHFD2 sits between methylene-THF and formyl-THF. The lack of an oxidative phosphorylation phenotype with MTHFD2 knockout led us to hypothesize that methylene-THF is the required 1C species. Consistent with this, SHMT2 knockout cell lines showed unchanged n-terminal f-Met levels of the mitochondrially translated MTCO1 peptide[19] (Extended Data Fig. 4a). To confirm that methylene-THF is the required species, we generated SHMT2/MTHFD2 double deletion cells and supplemented them with methylglycine (sarcosine), which can produce mitochondrial methylene-THF via sarcosine dehydrogenase. While sarcosine is not a preferred 1C source and its feeding was insufficient to restore oxidative phosphorylation in SHMT2 single gene knockout cell lines, it fully restored oxidative phosphorylation in the SHMT2/MTHFD2 double knockout cells, in which drainage of methylene-THF to formyl-THF is blocked (Fig. 2b and Extended Data Fig. 4b). Thus, mitochondrial methylene-THF is required to maintain respiratory capacity.

Depletion of mitochondrial dTTP and/or accumulation of uridine nucleotides have been shown to induce mitochondrial respiratory chain deficiency by promoting mitochondrial DNA damage[17,20]. However, SHMT2 knockout cells showed no evidence of altered mitochondrial DNA copy number (Figure 2c and Extended Data Fig. 4c), deletions (Extended Data Fig. 4d), or mutations (Extended Data Fig. 4g, h see also Supplementary Table 1). Moreover, whole cell RNA-sequencing revealed normal transcript levels for mitochondrial-encoded respiratory chain protein subunits (Figure 2d, Extended Data Fig. 4e, f). Thus, the dependence of oxidative phosphorylation on SHMT2 reflects a requirement for mitochondrial methylene-THF for a purpose other than supplying local dTTP to maintain mitochondrial DNA.

Whereas the vast majority of the ~1,100 mitochondrial proteins are imported from the cytosol, 13 essential respiratory chain subunits are locally transcribed and translated[21]. These include components of complexes I, III, IV, and V, but not complex II. Based on the normal mitochondrial transcript abundances and complex II protein levels, we hypothesized that mitochondrial methylene-THF is required for local translation. Indeed, [^{35}S]-methionine incorporation assays showed reduced synthesis of certain complex I and IV subunits (Extended Data Fig. 5a). To further probe mitochondrial translation, we developed a protocol for mitochondrial ribosome profiling, based on digesting unprotected mRNA with the nuclease MNase, enriching the 55S-mitochondrial ribosome, and sequencing the protected footprints (Fig. 3a and Extended Data Fig. 5b). This approach achieved > 90% average mitochondrial transcript sequence coverage with an average depth of > 80 reads per codon (Supplementary Table 3; Extended Data Fig. 5c). In SHMT2 knockout cells, the distribution of ribosome-protected footprints showed pronounced stalling at defined codon positions (Fig. 3b and Extended Data Fig. 6a). This resulted in relatively fewer actively translating ribosomes (i.e. bound and not stalled) for certain subunits of respiratory chain complexes I, IV, and V (Extended Data Fig. 6b). Consistent with the ribosome profiling data,

enzymatic assays revealed decreased activity of complexes I, IV, and V (Extended Data Fig. 6c).

We next aimed to elucidate the cause of ribosomal stalling. The A-site coordinates of stalled ribosomes revealed striking ribosome accumulation in SHMT2 knockout cells at particular lysine and leucine codons: Lys^{AAG} and Leu^{UUG} (Figure 3c). This did not appear to reflect shortage of these amino acids or tRNAs in mitochondria, as much less stalling was observed at the corresponding Lys^{AAA} and Leu^{UUA} codons. Instead, it appeared to relate to difficulty reading the 3' codon guanosine of codons where the 3' position identity (purine vs. pyrimidine) determines the encoded amino acid ("split codon boxes", Extended Data Fig. 6d). Increased codon occupancy observed also for Trp^{UGG}, Glu^{GAG} and Gln^{CAG}, but not the corresponding codons with 3' adenosine. The sole exception was $Met^{AUG/AUA}$, where no stalling was observed. Decoding of A/G ending codons in split codon boxes is facilitated by methyl-derivative base modifications of the tRNA anticodon 5' nucleotide, allowing non-Watson-Crick base-paring with the codon 3' base[22] (Figure 4a). The mitochondrial $tRNA^{Met}$ anticodon has a 5' cytidine which is formylated with the 1C unit derived from S-adenosyl-methionine (SAM)[23]. In contrast, the mitochondrial tRNAs for Lys, Leu1, Trp, Glu, and Gln have uridine at the 5' anticodon position[24]. Mammalian cytosolic tRNAs with uridine at the anticodon 5' position are modified to produce 5-methoxycarbonylmethyluridine (mcm5U), with the methoxy carbon from SAM[25,26]. Corresponding mitochondrial tRNAs are also modified at the 5' anticodon uridine (position 34 in the tRNA), which is 5-taurinomethyl modified (τm5U)[27–29]. As SHMT2/MTHFD2 double knockout cell lines supplemented with sarcosine showed rescue of codon specific stalling on mitochondrial ribosome profiling (Extended Data Fig. 6e), we hypothesized that the 5-taurinomethyl modification is dependent on mitochondrial methylene-THF and that the observed oxidative phosphorylation defect is a consequence of impaired translation due to defective tRNA modification.

To test this hypothesis, we established a liquid chromatography-mass spectrometry (LC-MS) method for detection of modified mitochondrial tRNA bases. In SHMT2 knockout cell lines, formylcytidine levels were unchanged (Extended Data.Fig. 7a). In contrast, τm5U and its 2-thio derivative (where the uracil 2-position oxygen is replaced with sulfur) were depleted to undetectable levels (Figure 4b; Extended Data Fig. 7b). The depletion was not due to lack of taurine, whose cellular levels tended to be higher (Extended Data Fig. 7c). The loss of τm5U and its 2-thio derivative was reversed upon re-expression of wild-type SHMT2 and also upon sarcosine supplementation of SHMT2/MTHFD2 double knockout cells (Extended Data Fig. 7d, e). Thus, SHMT2 or an alternative source of mitochondrial 5,10-methylene-THF is required to make τm5U.

To verify that the methyl group of τm5U is coming from 5,10-methylene-THF made by SHMT2, we conducted stable isotope tracing with [^{13}C]-labeled serine (the SHMT2 substrate) versus [^{13}C]-methionine (which feeds into SAM). As expected, methionine labeled formylcytidine. In contrast, serine but not methionine labeled τm5U (Extended Data Fig. 7f). Thus, SHMT2 is required for oxidative phosphorylation because it produces mitochondrial methylene-THF for tRNA taurinomethylation. To our knowledge, this is the first direct evidence of folate-dependent macromolecule modification in mammalian cells.

The enzyme complex catalyzing the τm5U base modification in mitochondria comprises two proteins, MTO1 and GTPBP3, both of which are human mitochondrial disease genes[30,31]. Its orthologues, forming the prokaryotic tRNA modifying MnmE/GidA complex, have been shown to use THF-bound 1C units[32]. We therefore explored if the mitochondrial translation defect upon SHMT2 loss matches human diseases proposed to affect taurinomethylation of mitochondrial tRNAs[27,28,30,31]. Indeed, MTO1 knockout in HCT116 cells caused loss of τm5U (Extended Data Fig. 7e). Mitochondrial ribosome profiling of these engineered MTO1 deletion cells showed an increase in codon occupancy at the same codons as with SHMT2 knockout (Figure 4c). In both cases, the strongest stalling occurred at Lys^{AAG} and Leu^{UUG}, potentially because these codons have, in addition to the wobble base pairing, only A-U base pairings versus the stronger C-G base pairings in Glu^{GAG}, Gln^{CUG} and Trp^{UGG} codons[33]. Mitochondrial ribosome profiling of primary fibroblasts of two patients carrying different *MTO1* missense mutations revealed increased codon occupancy selectively at Lys^{AAG}, but not Leu^{UUG}. Thus, these hypomorphic mutations seem to cause a selective defect in taurinomethylation of the Lys tRNA. Of all adenosine ending codons, Lys^{AAA} showed the greatest increase in codon occupancy across all cell lines, being most pronounced in the MTO1 patients (Figure 4c).

Intriguingly, in both SHMT2 and MTO1 deletion cells, stalling did not affect all AAG/UUG codons uniformly, but occurred most strongly at the same specific gene locations. Thus, stalling depends not only the defective codon-anticodon interaction, but also the transcript position or surrounding mRNA context (Extended Data Fig. 7g). Mapping of AAG/UUG codons at stalling sites relative to mRNA secondary structure[34] did not reveal any clear pattern (Extended Data Fig. 8a, b and Supplementary Table 4, 5). Mapping onto the structure of the protein being synthesized (Extended Data Fig. 8c), however, showed a trend towards enrichment for stalling at transitions between transmembrane helices and non-membrane domains (Supplementary Table 5). Thus, stalling due to the defective codon-anticodon interaction might be exacerbated by particular protein sequence features.

Defined mutations in the Lys and Leu1 mitochondrial tRNAs (which decode the most strongly affected Lys^{AAG} and Leu^{UUG} codons) result in a tRNA-specific τm5U modification defect, causing the human mitochondrial disorders MERRF and MELAS[27,28]. Mitochondrial ribosome profiling of fibroblasts from two *MT-TL1* m.3243A>G MELAS patients revealed, as expected[35], increased occupancy at Leu^{UUG} but not Lys^{AAG} or Leu^{UUA} (Figure 4d). For unknown reasons, increased ribosome occupancy for either Ser^{AGU} or Thr^{ACG} was also observed in individual patients (Extended Data Fig. 9a). The extent of stalling and complex I depletion was less than with nuclear *SHMT2* or *MTO1* mutations, presumably due to the heteroplasmic nature of the mitochondrial tRNA mutation (Figure 4c, Extended Data Fig. 9b). Collectively these observations highlight a common biochemical mechanism that links mitochondrial folate metabolism with a significant fraction of inborn mitochondrial diseases[27,28,30,31].

Based on these observations, we were curious whether folate deficiency, which in pregnancy causes neural tube defects[1–3], could also result in mitochondrial impairment. Consistent with such a possibility, growth of HCT116 wild-type cells in folate-deficient media resulted in decreased complex I enzyme levels and reduced basal respiration rate (Figure 4d and

Extended Data Fig. 10a), without impacting mitochondrial DNA content (Extended Data Fig. 10b). In individuals with adequate nutrition, functional folate deficiency can be caused by antifolate therapy for autoimmunity or cancer. Low doses of the antifolate methotrexate, resulting in up to 100 nM circulating drug concentrations, are commonly used to treat autoimmune diseases such as rheumatoid arthritis[4,36]. In cell culture, nanomolar concentrations of methotrexate resulted in decreased complex I enzyme levels and oxygen consumption (Figure 4d, Extended Data Fig. 10c). Thus, the essential role for folate metabolism in mitochondrial translation may contribute to the clinical manifestations of folate deficiency and the clinical efficacy of antifolate therapies.

Methods

Cell lines and growth conditions

HCT116 (CCL-247) and HEK293T/17 (CRL-11268) were purchased from ATCC®. Generation of a subset of clonal CRISPR/Cas9 knockout cell lines and detailed characterization has been reported previously[9]. Additional clonal knockout cell lines (Supplementary Table 6a) were established following the protocol published by Ran and colleagues[38]. In brief, exon targeting guide RNAs (Supplementary Table 6b) were designed against genes of interest and cloned into an expression vector containing the double nicking Cas9 variant (Addgene). Cells were transiently transfected using Lipofectamine 2000 (Life Technologies) (HEK293T) or Fugene HD (Promega) (HCT-116) and selected for 48 h with 2 μg/mL puromycin. Single clones were isolated using serial dilution into 96-well plates.

Stable SHMT2 re-expression was achieved by transfecting HEK293T knockout cell lines with NM_005412.5 cDNA (GE-Healthcare) cloned into pCMV-Tag8 vector (Agilent) and selection for three weeks with 200 μg/ml Hygromycine B (Sigma-Aldrich). Catalytic inactive (p.Glu98Leu/p.Tyr106Phe)[39,40] and PLP -binding deficient (p.Lys280Gln)[41] mutants were obtained following the QuickChange II protocol (Agilent). Knockout and re-expression cell lines were functionally verified by immunoblotting followed by targeted genomic sequencing (Supplementary Fig. 9) and, in the case of SHMT2 cell lines, also by tracing of [2,3,3 ^{2}H]-serine labeling into dTTP. MTO1 and MT-TL1 patient fibroblasts and controls were provided by the Department of Pediatrics, Salzburger Landeskliniken and Paracelsus Medical University, Salzburg. Studies with primary human cell lines were approved by the local ethics-committee and informed consent was obtained from all subjects. Genotype of MTO1 deficient patients (GenBank NM_012123.3) was as follows: pat_a c.[1261-5T>G];[1430G>A], (p.[?];[Arg477His]); pat_b c.[1222T>A];[1222T>A], (p.[Ile408Phe]; [Ile408Phe]). Patient MTO1_pat_b has been reported before[42]. Both MELAS patients carried the common *MT-TL1* m.3243A>G mutation with the heteroplasmy rate reported in this study. All cell lines tested negative for mycoplasma and were cultured in DMEM without sodium pyruvate (Sigma-Aldrich) supplemented with 10% dialyzed fetal bovine serum (dFBS, GE Healthcare) in a 5% CO_2 incubator at 37 °C. No antibiotics were used.

Glucose uptake and lactate secretion

Cells were seeded in 6-well plates 24 h before the start of an experiment. After reaching 50% confluency, plates were washed with phosphate buffered saline (PBS, GE Healthcare) and 3 ml of fresh media was added. Glucose uptake and lactate secretion were determined using an YSI 2900D Biochemistry Analyzer (Xylem Analytics) and normalized to cell growth as determined by µl packed cell volume (PCV, as measured using packed cell volume microfuge tubes from TPP).

Proliferation

Proliferation assays were conducted in 96-well plates and relative cell number was measured using resazurin sodium salt. 5,000 cells were plated in each well with 150 µl DMEM supplemented with 10% dFBS. Cell growth at each day was read as fluorescence intensity using a Synergy HT plate reader (BioTek Instruments).

Oxygen consumption

Oxygen consumption rates (OCR) were measured on a XF24 extracellular flux analyzer (Agilent) following the manufacturer's instructions. In brief, XF24 cell culture microplates were coated with fibronectin (Sigma-Aldrich) and cells were seeded at 5×10^4 (HEK293T) and 7×10^4 (HCT116) cells per well. After reaching 70-90 % confluency, cells were equilibrated for 1 h in XF assay medium supplemented with 10 mM glucose, 1 mM sodium pyruvate, and 2 mM glutamine in a non-CO_2 incubator. OCR was monitored at baseline and throughout sequential injections of oligomycin (1 µM), carbonyl cyanide-4-(trifluoromethoxy)phenylhydrazone (1 µM) and rotenone/antimycin A (0.5 µM each). Data for each well were normalized to cell number as determined by CyQUANT® Cell Proliferation Assay Kit (Invitrogen) and to the on-plate wild-type control. For absolute OCR values protein concentration was determined by BCA protein assay (Thermo Fisher Scientific).

Immunoblotting

Cells were cultured to sub-confluency in 6 cm plates. After removal of media, cells were rinsed with 4°C PBS and lysed in radio-immunoprecipitation assay (RIPA) buffer with phosphatase and protease inhibitors (Roche). Lysates were cleared by 10 min centrifugation at 16,000 × g and quantified using a BCA assay (Pierce). Samples were resolved by sodium dodecyl sulfate–polyacrylamide gel electrophoresis on precast gels (Bio-Rad) and transferred to a nitrocellulose membrane using the Trans-Blot Turbo system (Bio-Rad). After overnight incubation with primary antibodies, bands were visualized with horseradish peroxidase-conjugated secondary antibodies (Cell Signaling Technologies). ChemiDoc™ XRS+ system was used for image acquisition. The following antibodies were used according to their manufacturer's directions: Anti-SHMT1 (12612), SHMT2 (12762), MRPL11 (2066), S6RP (2217) and β-actin (5125) were from Cell Signaling Technologies; Anti-MTHFD2 (ab151447), NDUFS4 (ab139178), SDHA (ab14715) and VDAC (ab14734) were from Abcam Inc.; Anti-MTHFD1L (HPA029041) was from Sigma-Aldrich.

Analysis of mitochondrial specific translation

[^{35}S]-labeling of mitochondrial proteins was performed following the method described by Sasarman and Shoubridge[43]. In brief, cells were grown on 6 cm plates for 48 h to sub-confluency. Then media was changed to DMEM with 10 % dFBS without methionine (MP Biomedicals). Following a 30 min incubation, cytosolic translation was inhibited by emetine hydrochloride (0.1 mg/ml, Sigma-Aldrich) and labeling was conducted for one hour after the addition of 500 μCi [^{35}S]-methionine (EasyTag™ L[^{35}S]-Methionine, Perkin Elmer). Protein lysates (30 μg) were then separated on a 15% polyacrylamide gel (8.3 × 7.3 cm) and dried using a 443 Slab Dryer (BioRad). The dried gel was exposed to a storage phosphor screen (GE-Healthcare) and imaged on a Typhoon FLA 9500 (GE-Healthcare). Equal sample loading was confirmed by Coomassie brilliant blue staining (Biorad).

Metabolite concentrations and labeling patterns

Cells were grown in 6 cm dishes for at least 48 h and collected at 75% confluency. Media was replaced every 24 h and additionally 6 hrs before harvesting. Metabolism was quenched and metabolites were extracted by aspirating media and immediately adding 1 ml of 80:20 methanol:water at −80 °C. Plates were kept on ice, scraped and non-soluble debris was pelleted at 18,000 × g for 10 min. Samples were directly analyzed by hydrophilic interaction chromatography coupled with negative-mode electrospray-ionization high resolution mass spectrometry on a quadrupole-orbitrap scanning from m/z 73 to 1,000 at 1 Hz and 140,000 resolution (Q Exactive Plus, Thermo-Fisher). LC separation was achieved on a XBridge BEH Amide column (2.1 mm × 150 mm, 2.5 μm particle size, 130 Å pore size; Waters) using a gradient of solvent A (20 mM ammonium acetate + 20mM ammonium hydroxide in 95:5 water:acetonitrile, pH 9.45) and solvent B (acetonitrile). Flow rate was 150 μl/min. The gradient was: 0 min, 85% B; 2 min, 85% B; 3 min, 60% B; 9 min, 60% B; 9.5 min, 35% B; 12 min, 35% B; 12.5 min, 0% B; 18 min, 0% B; 18.5 min, 85% B; 23 min, 85% B. Data were processed and analyzed using in-house MAVEN software[44]. All isotope tracer experiments were conducted at isotopic steady state: [2,3,3-^{2}H]-serine was traced into dTTP for a minimum of 6 h and [3-^{13}C]-serine and [U-^{13}C]-methionine were traced into tRNA for a minimum of 4 days. Isotopic tracers were purchased from Cambridge Isotope Laboratories. Isotopically labeled media was prepared from scratch and supplemented with 10% dFBS.

RNA seq

RNA was isolated from cell lines using RNeasy Plus kit (Quiagen) according to the manufacturers´ recommendation. Following the depletion of ribosomal RNA libraries were prepared according to the TruSeq Stranded Total RNA protocol (Illumina) and sequencing was performed on a HiSeq 2500 (Illumina). Analysis was performed using the Galaxy system[45] and the R software package[46]. Adapter sequences were trimmed using Cutadapt (Galaxy version 1.6)[47] and the trimmed reads were then mapped with TopHat (Galaxy Version 0.9)[48] to the GRCh38 reference using ENSEMBL version 80 genes as known splice junctions. The read counts per gene were determined using htseq-count (Galaxy Version 0.6.1galaxy1)[49] in ‘union’ mode. Differential expression analysis was performed in R using DESeq2 1.12.3 package[50]. SHMT2 knockout gene expression (log2 reads per kilobase of

transcript per million mapped reads (RPKM)) was graphed relative to the wild-type and the re-expressed cell lines.

Mitochondrial DNA content and integrity

To analyze mitochondrial DNA content, total DNA was extracted from 7×10^6 cells using Gentra Puregene Cell Kit (Quiagen) after freezing the cell pellet at -80°C for 1 h and overnight digestion with Proteinase K (Roche Diagnostics). Quantitative real-time PCR (ViiA 7, Applied Biosystems) was performed using primers targeting the mitochondrial ND2 locus (fwd: TGTTGGTTATACCCTTCCCGTACTA; rev: CCTGCAAAGATGGTAGAGTAGATGA) and a nuclear ALU repeat sequence (fwd: CTTGCAGTGAGCCGAGATT; rev: GAGACGGAGTCTCGCTCTGTC) as published earlier[51]. The relative mitochondrial DNA content was determined using the ΔΔCt method. Each independent sample given in the figures represents the mean of 6 technical replicates.

The mitochondrial genome was screened for deletions by long range PCR with two primer pairs spanning the whole coding region (fwd_1: CCAACCAAACCCCAAAGAC, rev_1: TACTGCGACATAGGGTGCTC; fwd_2: CACCAGCCTAACCAGATTTCA rev_2: TGGTACCCAAATCTGCTTCC) and products run on a 1% agarose gel[52]. DNA from a mitochondrial DNA deletion patient was used as positive control.

For mitochondrial genomic sequence analysis, mtDNA was enriched using the multiple displacement amplification strategy (REPLI-g, Quiagen) and sequencing was performed on a HiSeq 2500 after library preparation following the Nextera library prep kit protocol (Illumina). Reads were mapped to GRCh38 using Bowtie2 (Galaxy Version 0.6)[53] with default settings. Coverage plots were generated using DeepTools bamCoverage (Galaxy Version 2.3.6.0)[54]. The data were normalized to 1× coverage using an effective genome size of 16,569. Freebayes (Galaxy Version 0.4.1)[55] with frequency-based pooled settings was used to generate the variant data. The figures were generated in R using Gviz 1.18.0[56].

MT-TL1 mutation load was determined using primers specifically spanning the m.3243 position for targeted enrichment (fwd: AATGATACGGCGACCACCGAGATCTACACNNNNNNGCCTTCCCCCGTAAATGATA, rev: CAAGCAGAAGACGGCATACGAGATCGTCAGCGAAGGGTTGTAGT) followed by sequencing on a MiSeq nano flow cell using a custom sequencing primer (seq: TATTATACCCACACCCACCCAAGAACAGGGTTTGTTAAG). Alignment to GRCh38 was performed using Bowtie2 (Galaxy Version 0.6)[53] at default settings and position specific mutation load was derived from the Integrative Genomics Viewer.

Mitochondrial ribosome profiling

Development of our ribosome profiling method was based on concepts reported by other groups[57–59]. For mitochondrial ribosome profiling, cell lines were grown on 15 cm plates to 70-85% confluency. Sarcosine rescue of ribosome stalling in the SHMT2/MTHFD2 double-knockout background was assessed after growth in the presence of 1 mM sarcosine for 5 days. After removal of media, plates were rapidly rinsed with ice cold phosphate buffered saline containing chloramphenicol (100 μg/ml) (Sigma-Aldrich) and cycloheximide (100 μg/ml) (Sigma-Aldrich) followed by immediate immersion into liquid nitrogen. Plates were

then transferred to wet ice and 1 ml of 1.5× lysis buffer was added and the lysate was collected using a cell scraper. Lysis buffer contained the following: 1.5% triton X-100 (Sigma-Aldrich), 0.15% NP40 (Sigma-Aldrich), 1× complete phosphatase and protease inhibitors (Roche), and 30 U/ml DNase 1 (Roche) in buffer base (20 mM Tris–HCl pH 7.8 (Ambion), 100 mM KCl (Ambion), 10 mM $MgCl_2$ (Ambion), 100 μg/ml chloramphenicol, 100 μg/ml cycloheximide). 1.6-1.8 ml were recovered per plate and homogenized by passing three times through a 32G needle at 4°C. Non-soluble debris was pelleted at 5,000 g for 10 min and 1,520 μl supernatant was used for digestion with 2,250 U Micrococcal nuclease (Roche) after adding 40 μl SUPERaseIN (Ambion) and 5 mM CaCl2 (Ambion). Digest was stopped after 1 h gentle shaking at 25°C using a final concentration of 6 mM EGTA.

Buffer base was used to make 5% - 45% sucrose gradients (Gradient Master, Biocomp). After cooling to 4°C, samples were separated in an ultracentrifuge using the SW-41Ti rotor at 35,000 rpm for 2.5 h. Live UV absorption at 254 nm was used to track the mitochondrial 55S monosome enriched fractions (Extended Data Fig. 5b). The 55S fractions were pooled and mixed with 57 μl 20% SDS per ml sample before performing acid phenol chloroform RNA extraction. RNA was precipitated using 300 mM sodium acetate pH 5.5 and equal volume isopropanol and run on a 15% TBE-urea gel (Invitrogen) at 210 V for one hour for size selection. Gels were stained with Sybr® Gold (Invitrogen) and RNA fragments corresponding to mitochondrial ribosome footprints (~28-40 nucleotides) were cut and recovered from the gel using the crush and soak method. After sodium acetate/isopropanol precipitation library preparation was conducted following the TruSeq® Ribo Profile (Illumina) protocol.

Sequencing of ribosome protected footprints (RPFs) was performed on a HiSeq 2500 in rapid mode followed by adapter trimming using Cutadapt (Galaxy Version 1.6)[47]. Reads were mapped to the human genome reference GRCh38 using BWA (Galaxy Version 0.9)[48] with those mapping to the mitochondrial protein-coding genes included in the subsequent analysis. The Plastid package[60] and customized Phyton and R[46] scripts were used for analyzing mitochondrial ribosome profiling data. Alignment was performed from 3`of reads which was reported to yield superior results after digestion with Micrococcal nuclease[61,62]. Each read, corresponding to a mitochondrial ribosome protected fragment (mtRPF), was assigned to a nucleotide position representing the respective ribosomal A-site as determined by metagene analysis[60]. mtRPF counts were then normalized to reads per million (RPM) mapped reads within each sample and single nucleotide positions were grouped by codon index. This transformation allows for relative quantification of bound ribosomes for each nucleotide triplet along a transcript. Stalling plots were created by plotting the mean cumulative mtRPF count along each mitochondrial open reading frame.

Codons were defined as stalling sites when the normalized counts mapped to the specific codon (mtRPFcodon/mtRPF gene median) exceeded 2 standard deviations from all codons in the genome. The relative abundance of actively translating ribosomes (i.e. not stalled) was calculated by subtracting mtRPF counts in stalled regions from the total sum of ribosome footprints for each gene as $\Sigma mtRPF_{active} = \Sigma mtRPF_{total} - \Sigma mtRPF_{stalled}$. Then the gene specific ratio was plotted as $\Sigma mtRPF_{active,\ \Delta SHMT2} / \Sigma mtRPF_{active,wild\text{-}type}$. Stalling sites specific to the SHMT2 knockout condition were identified using the ratio of occupancy at

each codon position relative to wildtype. Specifically, codons were defined as SHMT2-specific stalling sites when the normalized counts in the mutant relative to WT (ΣmtRPFcodon $_{\Delta SHMT2}$/ΣmtRPF codon$_{wild\text{-}type}$) exceeded 2 (or, as indicated, 3) standard deviations from this ratio as determined for all codons in the genome, and the site also met the general stalling site criterion.

To determine the relative abundance of mitochondrial ribosomes bound to each nucleotide triplet, codon-specific occupancy ratios were calculated. For each codon (codon$_{i=1\text{-}64}$), the gene-specific ratio between experimentally measured ribosome density and expected density (which is proportional to codon frequency) was calculated. Codon occupancy (CO $_{i=1\text{-}64}$) for each codon is the mean of the ratios from all 13 genes. The relative codon occupancy (CO $_{i=1\text{-}64,\Delta SHMT2}$)/(CO$_{i=1\text{-}64,wild\text{-}type}$) was plotted with error bars representing standard deviation across replicates after error propagation. To investigate the ribosome distribution relative to the major stalled codons (AAG and UUG), ribosome densities flanking the codons of interest within 25 amino acids were selected. Each selected fragment was first normalized to its total count so every codon of interest from the genome is weighted equally. The mean value from each position was plotted. All sequencing data presented in this manuscript, except for ribosome profiling of primary patient cell lines, has been submitted for public availability to the sequence read archive submission code SUB2743534.

Investigating protein secondary structure effects on stalling at AAG/UUG

On average stalling was most pronounced at AAG and UUG codons, but not all codons of the same sequence were equally affected. We therefore investigated whether the positioning relative to protein secondary structures (transmembrane helices) influences the extent of stalling. As Micrococcal nuclease treatment induces imprecision in A-site mapping due to sequence-biased digestion[63,64], individual positions identified as SHMT2-specific stalling sites were first grouped to the adjacent codons decoded by 5-taurinomethyluridine-modified tRNAs. Then amino acid residues corresponding to the AAG/UUG codons were mapped to Bos taurus crystal structures of mitochondrial respiratory chain complex proteins using iCn3D[65]. Structure data was retrieved using the following PDB IDs: ATP6: 5ARA_W; MT-CO2: 2Y69_B; MT-CYB: 1QCR_C; and MT-ND6: 5LDW_J. Additionally, a hidden Markov model based algorithm for transmembrane helices (TMHMM 2.0[66]) was used to predict alpha helical transmembrane domains in the Homo sapiens sequences. This method assigns each codon a probability for transmembrane helix localization which was then used for genome wide assessment of AAG/UUG localization relative to transmembrane helices. AAG/UUG codons were defined to be at a transition between a transmembrane helix and a non-membrane region if, within the five flanking codons, probabilities > 0.5 and < 0.5 for being in a transmembrane helix are found. AAG/UUG codons were defined as stalling sites based on the 3 SD cut-off as per Extended Data Figure 8b. In total, 4/5 stalling AAG/UUG and 7/23 non-stalling AAG/UUG were at a membrane transition ($p = 0.04$ by Chi-square).

Evaluation of mRNA secondary structure effects on ribosome stalling

To study a potential effect of mRNA secondary structure[67] (i.e. base pairing) on ribosome stalling we used the previously published dimethyl sulfate sequencing datasets on human K562 cell lines from Rouskin et al.[34] to identify structured regions in mitochondrial

transcripts. Following the methods described in the manuscript for nuclear transcripts, identification of sites with secondary structure was performed on mitochondrial transcript data[34]. In brief, FASTQ files (accession no. GSM1297495, GSM1297493) were retrieved from sequence read archive and mapped to GRCh38 with BWA (Galaxy Version 0.9)[48]. Reads were assigned to the nucleotide at the five-prime end with no offset using Plastid[60]. R-value (cutoff 0.75) and Gini differences (cutoff 0.1) between the *in vivo* and denatured dataset were calculated for the complete mitochondrial transcriptome for a window size of 50 adenosine/cytosine nucleotides and a step size of 10. This provided a list of structured mitochondrial transcript regions, with most mRNA regions unstructured. The list of structured regions was compared to the SHMT2-specific stalling sites for potential co-localization. No stalling site mapped to a structured region.

Mitochondrial enzyme activities

Activities of individual OXPHOS complexes I-IV, ATP synthase and citrate synthase (CS, which is nuclear encoded and was used as a marker of mitochondrial mass) were spectrophotometrically measured as previously described (Uvicon 922, Kontron)[68–70]. Measurements were performed with 2 μl of mitochondria isolated by differential centrifugation[71] (except for complex I, where 10 μl was used).

CS (EC 2.3.3.1) activity was determined following extinction dynamics at 412 nm, indicating the cleavage of Elman´s reagent (0.2 mM) after addition of oxaloacetate (0.5 mM) to the buffered reaction solution containing acetyl-CoA (0.15 mM). Rotenone-sensitive complex I (NADH:decylubiquinone oxidoreductase, EC 1.6.5.3) activity was measured by adding NADH (0.2 mM) and monitoring at 340 nm for the reduction of decyl-ubiquinone (50 μM). Complex II (succinate:ubiquinone-oxidoreductase, EC 1.3.5.1) was measured at 600 nm by monitoring the reduction of 2,6-dichlorophenol-indophenol (80 μM) after addition of succinate (10 mM). The reaction mixture to determine complex III activity (coenzyme Q:cytochrome c—oxidoreductase, EC 1.10.2.2) contained cytochrome c (100 μM) and decyl-ubiquinol (200 μM) and was measured at 550 nm. After inhibition by addition of antimycin A (1 μM) the insensitive activity was subtracted to calculate specific complex III activity. The enzyme activity of complex IV (ferrocytochrome c:oxygen oxidoreductase, EC 1.9.3.1) was read as the oxidation rate of reduced cytochrome C (60 μM) at 550 nm. Complex V (F_1F_0 ATP synthase, EC 3.6.3.14) was indirectly measured as oligomycin-sensitive ATPase activity in a reaction mixture containing 0.5 mM ATP. Formed ADP was coupled to a pyruvate kinase reaction, utilizing phosphoenolpyruvate (2 mM) to generate ATP and pyruvate. The latter is then used by lactate dehydrogenase in the oxidation of NADH (0.2 mM) that served as direct readout (340 nm). Reagents were obtained from Sigma-Aldrich.

Mitochondrial tRNA modifications

HCT116 or HEK293T cell lines and sub clones were grown to 70-85% confluency and harvested for mitochondrial extraction ($1\text{-}2 \times 10^8$)[71]. Mitochondrial tRNAs were extracted using the MirVana™ miRNA Isolation kit (Ambion) for isolation of small RNAs followed by 10% TBE-urea gel purification and extraction as described above (tRNA fraction 65-85 bp). Quantitative analysis of 5-taurinomethyluridine monophosphate (tm5U), 5-

taurinomethy-2-thiouridine monophosphate (tm5s2U), 2-thiouridine monophosphate (s2U) and 5-formylcytidine monophosphate (f5C) was performed using high resolution mass spectrometry following a protocol adapted from[25,72]. In brief, 100 ng tRNA were digested at 37°C for 2 h by nuclease P1 (2 U) in 30 μl of 100 mM ammonium acetate and quenched by adding 60 μl 50/50 methanol/acetonitrile followed by centrifugation at 10, 000 g for 10 min. 5 μl of sample was injected for liquid-chromatography mass spectrometry analysis. Nucleoside monophosphates were analyzed on a quadrupole-orbitrap mass spectrometer (Q Exactive plus, Thermo Fisher Scientific) operating in negative ion mode coupled to hydrophilic interaction chromatography via electrospray ionization and used to scan in SIM mode from m/z 459 to 482 (tm5U and tm5s2U) or m/z 338 to 355 (s2U and f5C) at 1 Hz and 140,000 resolution. Consistent loading was ensured by measuring f5C levels (which are not altered by SHMT2 knockout) in the same sample as the tm5U and tm5s2U. The mass spectrometry standard for 5-taurinomethyluridine was synthesized as described by Ogata et al[73] and was used to confirm peak identity in digested tRNA samples after an additional treatment with 1 U of alkaline phosphatase (Roche) in 100 mM ammonium carbonate at 37°C for 2 h[72].

Folate depletion and methotrexate treatment

Cells were grown for five passages in folic acid-deficient DMEM with 10% dFBS (US Bio), either with or without HT supplement (Gibco), containing sodium hypoxanthine and thymidine at a final concentration of 100 μM and 16 μM respectively (1× HT). To evaluate the effect of targeting 1C-metabolism on mitochondrial function, methotrexate (Sigma-Aldrich) was used at 25, 50 and 75 nM concentration. Chloramphenicol (100 μg/m = 310 μM) and ethidium bromide (100 ng/ml = 250 nM) served as positive controls for the inhibition of mitochondrial translation and mtDNA depletion respectively. At each time point protein and DNA samples were collected for immunoblot and mtDNA content analysis. Basal respiration was assessed using the Seahorse XF analyzer with measurements conducted as described above.

N-terminal protein formylation

N-formyl methionine modification on MTCO1 (COXI) was assayed by mass spectrometry following the protocol of Tucker et al.[19]. In brief, mitochondria were isolated from cells by differential centrifugation[71] and complex IV was immunoprecipitated (ab109801, Abcam) before separation on a 4-20% polyacrylamide gel. A band running at the same molecular weight as a band reactive with an anti-MTCO1 antibody (ab14705, Abcam) was excised and lysed using 1.5 μg LysC (Wako) as described[74]. Samples were dried in a speedvac and re-suspended with 15 μl of 0.1% formic acid pH 3. Per run, 5 μl were injected using an Easy-nLC 1000 UPLC system. Samples were loaded directly onto a 45 cm × 75 μm nano-capillary column packed with 1.9 μm C18-AQ (Dr. Maisch) mated to a metal emitter (Thermo Scientific) in-line with a Thermo Orbitrap Elite or Thermo Orbitrap Lumos. The mass spectrometer was operated in data-dependent mode with the 120,000 resolution MS1 scan (400-1800 m/z) in the Orbitrap followed by up to 20 MS/MS scans in the ion trap. Raw files were searched using MSAmanada[75], Sequest HT[76] and Byonic[77] algorithms and validated using the Percolator algorithm[78] within the Proteome Discoverer 2.1 suite (Thermo Scientific). 10 ppm MS1 and 0.6 Da MS2 mass tolerances were specified.

Carbamidomethylation of cysteine was used as fixed modification and oxidation of methionine as dynamic modification. Additionally, acetylation, formylation and loss of methionine were specified as potential modifications at the n-terminus of proteins. The resulting msf file was used to construct a spectral library (percolator peptide q-value >0.95) and extract MS1 ion chromatographs in Skyline[79,80]. The fraction of modified n-terminal peptides of MT-CO1 was calculated as the area of the formylated peptide divided by the sum of the areas of all the n-terminal peptides in that sample.

Statistics and Reproducibility

Significance was determined by two-tailed Student's *t*-test comparing the indicated condition to the corresponding wild-type or control. *P* values <0.01 are indicated as *. Exact p-values for individual comparisons are given in Supplementary Table 7. Small filled circles are individual data points. All results have been independently replicated at least twice. This includes figure panels where representative data is shown. For quantitative measurements, n is provided in the figure legends. For western blots and DNA gels, we show representative data of multiple independent replicates: Fig. 1c (n = 2), Fig. 2b (n = 3), Fig. 4c (n = 3); Extended Data Figs. 1a (n = 2), 1h (n = 2), 1i (n = 2), 2b (n = 2), 2c (n = 2), 3a (n = 2), 4d (n = 2), 5a (n = 2), 5b (n = 3), 7f (n = 2), 10a (n = 3) and 10c (n = 2).

Code availability

All code used to generate the data in this manuscript is publicly available from GitHub.

Data availability

Raw sequencing data are available from Sequence Read Archive under BioProject accession number PRJNA419990. Source data for Fig. 1c, Fig 3c, Fig. 4C, Extended Data Fig. 3d and Extended Data Fig. 6e are provided with the paper. Uncropped versions of blots are given as Supplementary Fig. 1-8; Sanger sequencing traces as Supplementary Fig. 9. Other data that support the findings of this study are available from the corresponding author upon reasonable request.

Extended Data

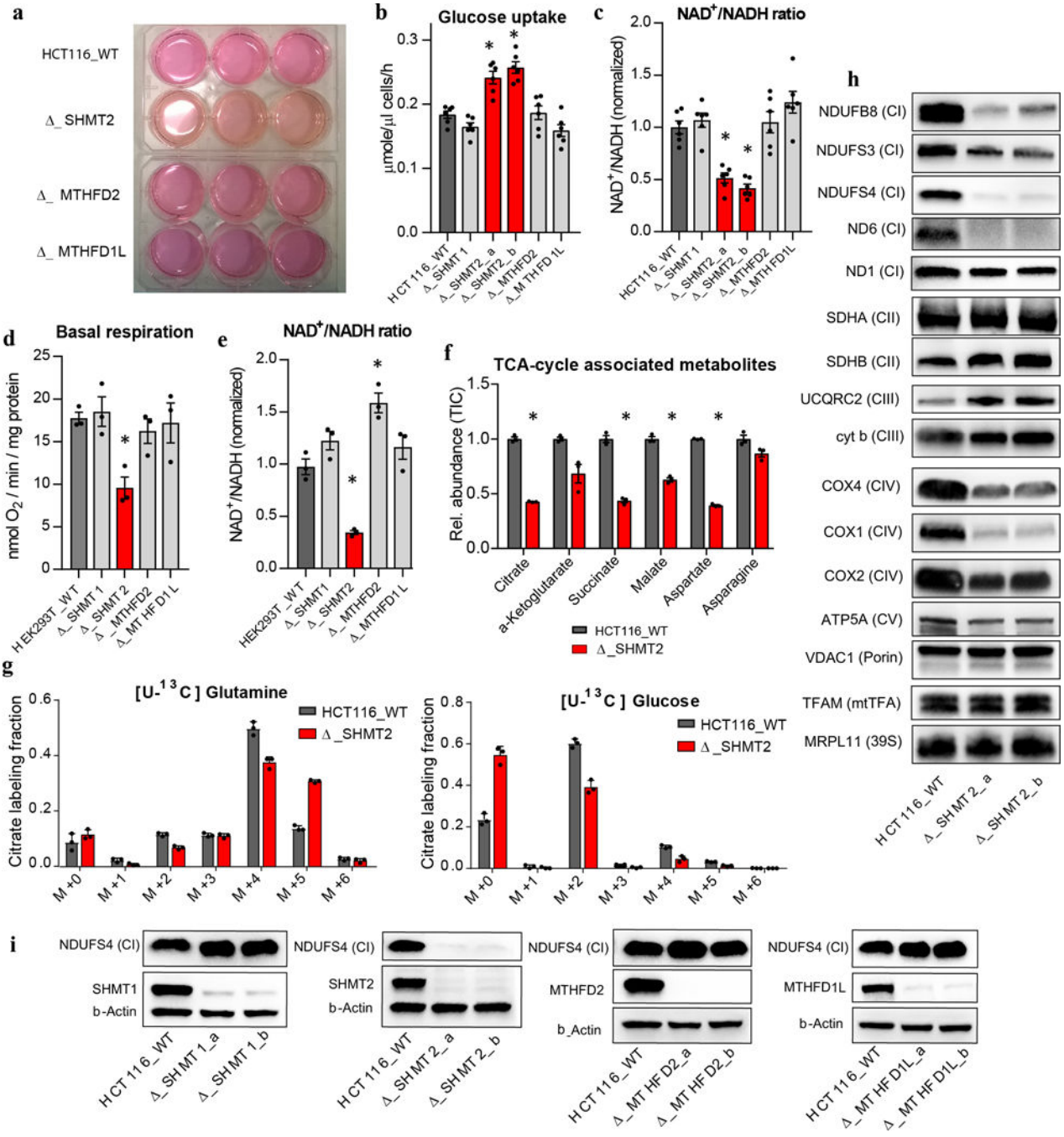

Extended Data Figure 1. SHMT2 deletion-induced respiratory chain dysfunction in different cellular backgrounds and clones

a, Change in media color after 48 h cell growth. **b**, Lactate secretion and **c**, normalized NAD$^+$/NADH ratio of HCT116 knockout cell lines ($n = 6$). **c**, Basal respiration of HEK293T folate 1C gene CRISPR/Cas9 knockout cell lines as measured by Seahorse XF analyzer ($n = 3$) and **e**, normalized NAD$^+$/NADH ratio ($n = 3$). **f**, Normalized levels of TCA-cycle and associated metabolites ($n = 3$). **g**, Steady-state labeling fraction into citrate from [U-^{13}C]-

substrates glutamine and glucose, respectively ($n = 3$). **h**, Immunoblot of extracted mitochondria for subunits of respiratory chain complexes I-V and markers of mitochondrial mass. **i**, Mitochondrial complex I levels (NDUFS4) in independent HCT116 folate 1C gene knockout clones. Results are given as mean ± s.e.m; n indicates the number of biological replicates. Significance is calculated by two-tailed Student´s t-test. * $P < 0.01$ (see Supplementary Table 7 for exact p values). Abbreviations: CI-V, respiratory chain complex I-V.

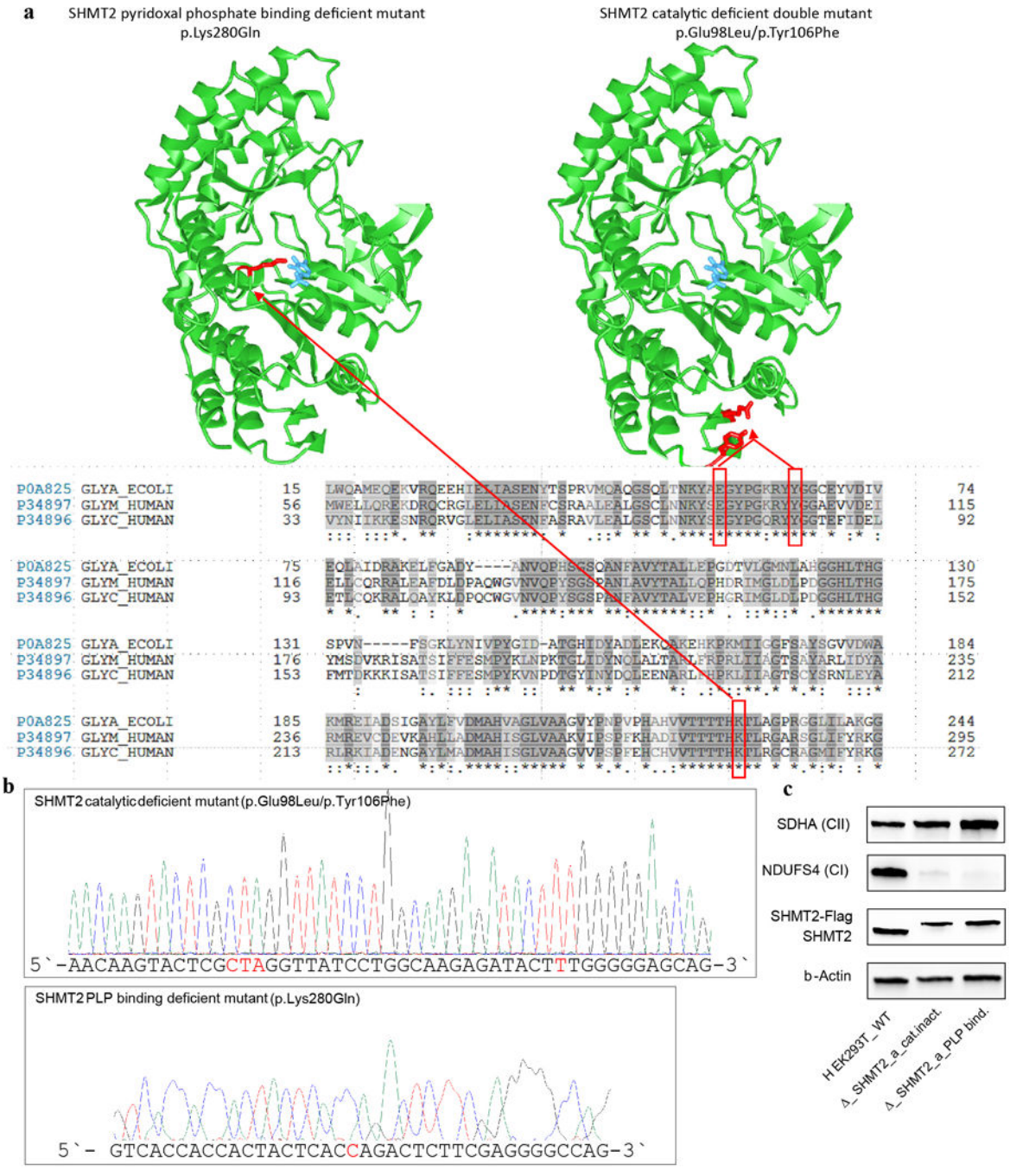

Extended Data Figure 2. Catalytically deficient SHMT2 constructs

a, Mapping of mutated amino acid residues on human SHMT1 (PDB code 1BJ4[81]) using iCn3D and alignment of E. coli serine hydroxymethyltransferase (GLYA), H. sapiens mitochondrial serine hydroxymethyltransferase 2 (GLYM) and cytosolic serine hydroxymethyltransferase 1 (GLYC). Positions for GLYM are given with reference to GenBank NM_005412.5. **b**, Sanger sequencing traces of mutant constructs. **c**, Immunoblot for mitochondrial complex I levels (NDUFS4) in cell lines re-expressing catalytically deficient forms of SHMT2.

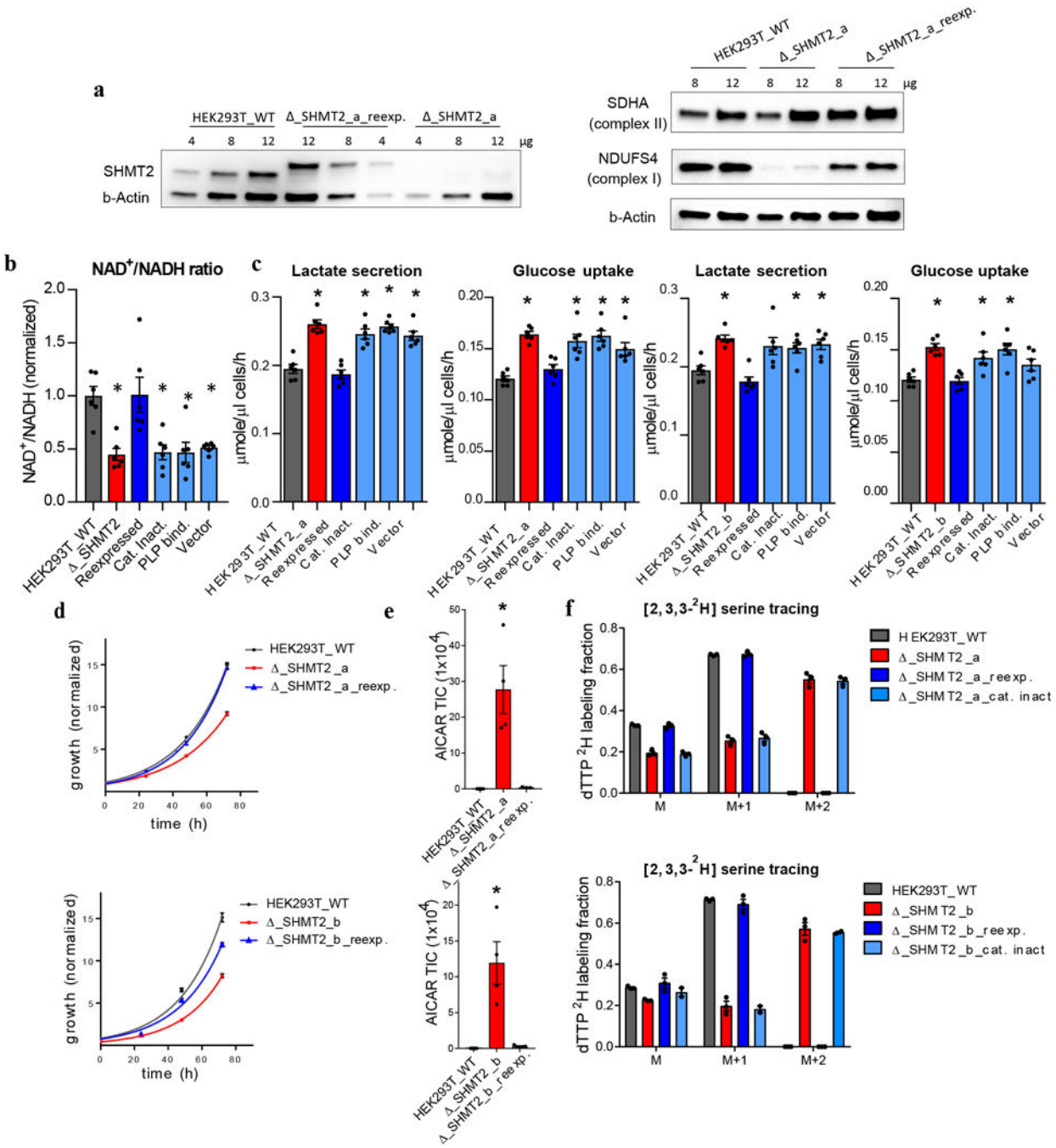

Extended Data Figure 3. Restoring SHMT2 catalytic activity is critical for normalizing one-carbon flux, respiratory chain expression, glycolytic activity, and cell growth

a, Immunoblot of re-expression of catalytically active SHMT2 and effects on mitochondrial complex I and II levels. **b-f**, Impact of re-expression of catalytically active and inactive forms of SHMT2 in the HEK293T background. **b**, Normalized NAD^+/NADH ratio ($n = 6$) **c**, lactate secretion and glucose uptake ($n = 6$), **d**, cell proliferation ($n = 6$). **e**, Purine biosynthesis intermediate 5-aminoimidazole-4-carboxamide ribonucleotide (AICAR) levels ($n = 4$) as an indicator of cytosolic folate 1C status, and **f**, [2,3,3-^{2}H]-serine tracing to

differentiate cytosolic from mitochondrial folate 1C unit production for incorporation into deoxythymidine triphosphate ($n = 3$). Results are given as mean ± s.e.m; n indicates the number of biological replicates. Significance is calculated by two-tailed Student´s t-test. * P <0.01 (see Supplementary Table 7 for exact p values).

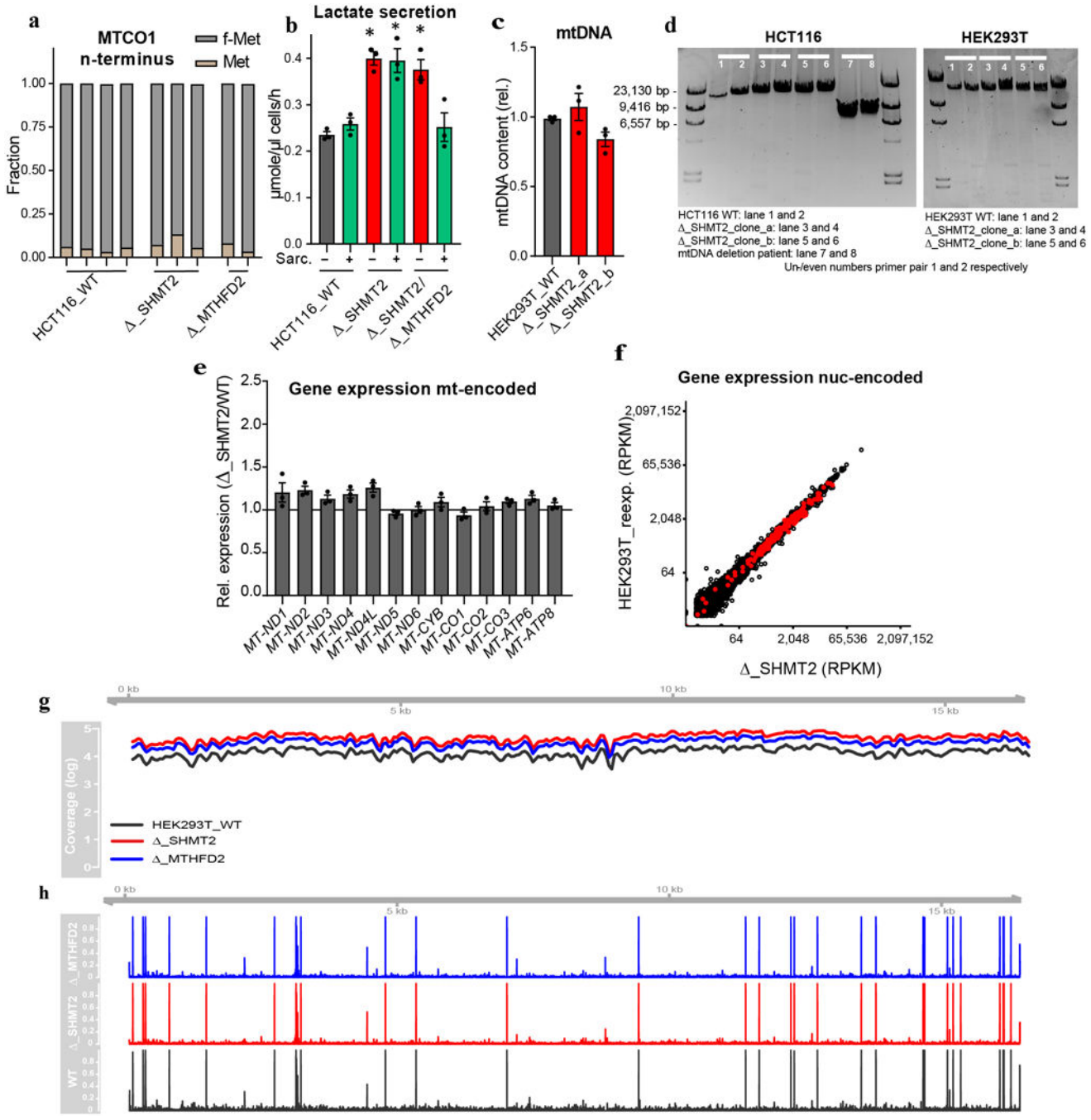

Extended Data Figure 4. Oxidative phosphorylation defect is caused by a post-transcriptional mechanism independent of methionine formylation

a, Fraction of initiating amino acid (formyl-methionine vs. methionine) of mitochondrial-expressed MTCO1 peptide determined by high resolution liquid-chromatography mass

spectrometry (WT $n = 4$, ΔSHMT2 $n = 3$, MTHFD2 $n = 2$). **b**, Lactate secretion ($n = 3$) upon sarcosine supplementation (1 mM). **c**, Relative mtDNA levels in HEK293T ($n = 3$). **d**, agarose gel of mtDNA long range-PCR products of HCT116 and HEK293T knockout cell lines. **e**, relative mRNA levels of mtDNA encoded respiratory chain subunits ($n = 3$). **f**, Gene expression levels in SHMT2 knockout cell lines compared to SHMT2 wild-type re-expressed lines by total RNA sequencing. Each dot represents mean gene expression as derived from two biological replicates of two independent knockout clones and matched re-expressed lines ($n = 4$). Genes linked to human OXPHOS function[37] are highlighted in red. Significantly differentially expressed genes are listed in Supplementary Table 2. **g**, Position dependent next generation sequencing coverage of mtDNA in HEK293T wild-type, SHMT2 knockout and MTHFD2 knockout cell lines supports the absence of deletions due to SHMT2 loss. **h**, Corresponding variant position and frequency. Variant list is given in Supplementary Table 1. Bar graphs show mean ± s.e.m; n indicates the number of biological replicates. Significance is calculated by two-tailed Student´s t-test. * $P < 0.01$ (see Supplementary Table 7 for exact p values). Abbreviations: mtDNA, mitochondrial DNA.

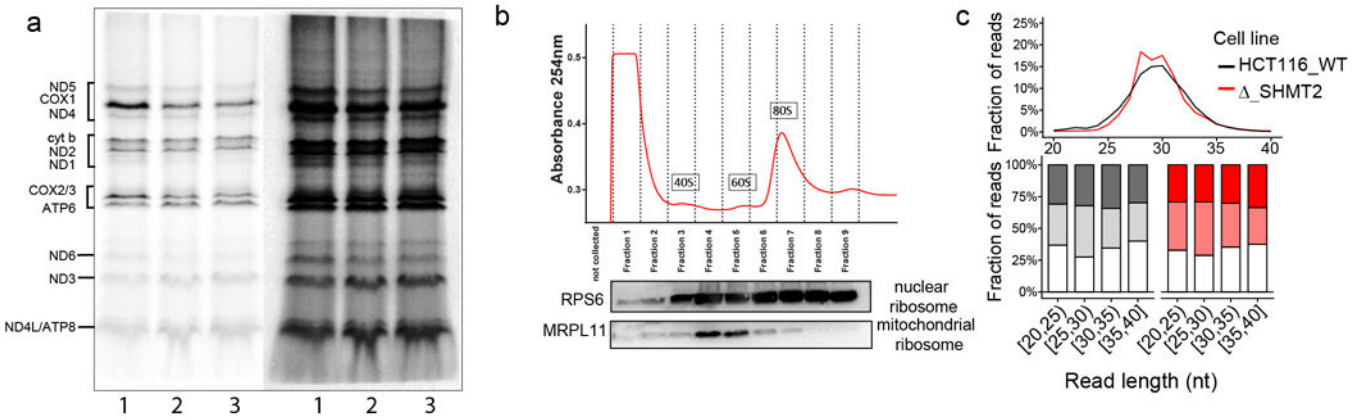

Extended Data Figure 5. Impairment of mitochondrial translation due to loss of SHMT2

a, SDS-PAGE of [^{35}S]-methionine labeled mitochondrially translated proteins in wild-type (lane 1) and two SHMT2 knockout HEK293T cell lines (lane 2, 3). Decreased synthesis of COX1 and COX2/3 are evident upon short exposure and reduced synthesis of ND5 and ND6 is more easily visualized upon longer exposure. **b**, Absorbance at 254 nm upon sucrose gradient fractionation of Micrococcal nuclease digested cell lysates (Figure 3a). Fractions corresponding to 4 and 5 were collected for mitochondrial ribosome enrichment as shown on the matched immunoblot for mitochondrial ribosome subunit MRPL11. **c**, Read length distribution (top) and read length-dependent sub-codon read phasing (bottom) across the 13 mitochondrial protein coding transcripts. Panel c is based on data from the mitochondrial ribosome profiling experiment displayed in main text Figure 3 and displays the mean of two technical replicates of two independent samples.

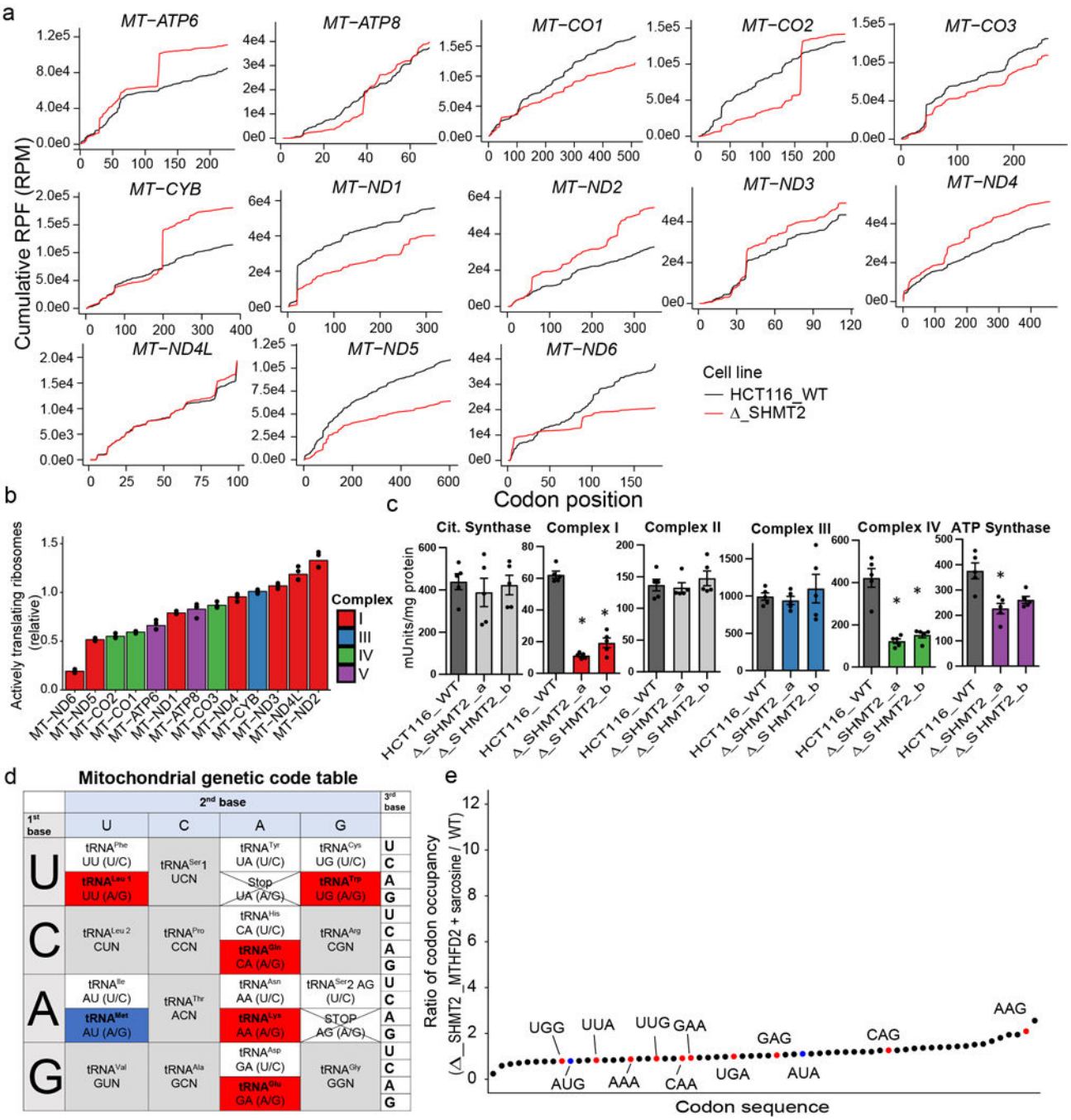

Extended Data Figure 6. Mitochondrial ribosome stalling at guanosine-ending split codon box nucleotide triplets suggests deficient 5-taurinomethyluridine modification

a, Expanded version of main text Figure 3b, in this case showing the mean cumulative ribosome protected fragments of all mitochondrial protein-coding genes. **b**, Mean relative density of actively translating (i.e. not stalled) ribosomes for mitochondrial transcripts. **a** and **b**, two technical replicates of two independent samples. **c**, Enzymatic activities of citrate synthase and individual mitochondrial respiratory chain complexes from mitochondrial extracts (n = 5). Bar graphs show mean ± s.e.m. Significance is calculated by two-tailed

Student´s *t*-test. * $P<0.01$ (see Supplementary Table 7 for exact p values). **d**, Mitochondrial genetic code table with split codon boxes depending on taurinomethylated tRNAs for translation highlighted in red. Codons decoded by anticodon formylcytidine-containing $tRNA^{Met}$ are highlighted in blue. **e**, Mean codon-specific mitochondrial ribosome occupancy of HCT116 SHMT2/MTHFD2 double knockout cell lines supplemented with sarcosine (1 mM). Codons highlighted in red are decoded by tRNAs carrying a 5-taurinomethyluridine modification. The supplementation with sarcosine prevents the stalling normally observed with SHMT2 deletion (n =2).

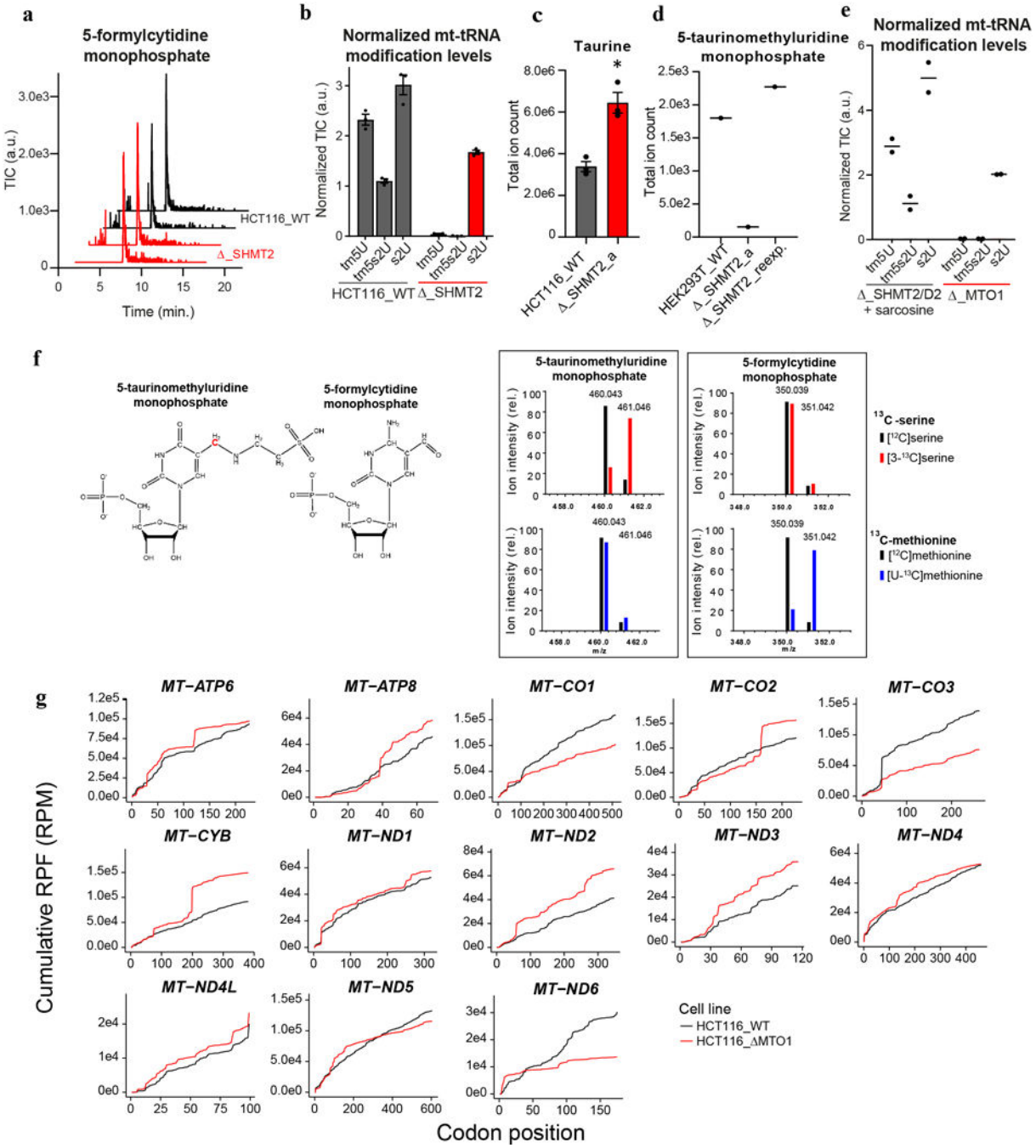

Extended Data Figure 7. tRNA modification status in ΔSHMT2 and effects of 5-taurinomethyluridine modification loss caused by human disease gene *MTO1*

a, Total ion chromatogram of 5-formylcytidine monophosphate in digested mitochondrial tRNAs upon loss of SHMT2. The same samples were analyzed for 5-taurinomethyluridine monophosphate (tm5U) in Figure 4b. The combined data demonstrate that SHMT2 deletion causes loss of tm5U but not 5-formylcytidine. **b**, levels of tm5U, 5-taurinomethyl-2-thiouridine monophosphate (tm5s2U) and 2-thiouridine monophosphate (s2U) in wild-type HCT116 and SHMT2 deletion lines normalized to 5-formylcytidine monophosphate (f5C)

(*n* = 3). **c**, Taurine levels in HCT116 wild-type and SHMT2 knockout cell lines (*n* = 3). **d**, tm5U levels in digested mitochondrial tRNAs upon re-expression of SHMT2 (*n* = 1). **e**, tm5U, tm5s2U and s2U levels normalized to f5C in HCT116 SHMT2/MTHFD2 knockout lines after sarcosine supplementation and HCT116 upon loss of MTO1 (*n* = 2). For all panels data is presented as mean ± s.e.m. or individual data points only. **f**, Labeling pattern of 5-taurinomethyluridine and 5-formylcytidine monophosphate extracted from mitochondrial tRNAs after growth in media containing either [3-^{13}C]-serine or [U-^{13}C]-methionine. **g**, Mean cumulative count of ribosome protected fragments (RPF) mapping to mitochondrial protein coding transcripts upon ribosome profiling in HCT116 MTO1 knockout cell lines. Data was normalized to reads per million (RPM) (*n* = 2); *n* indicates the number of biological replicates. Significance is calculated by two-tailed Student´s *t*-test * *P* <0.01 (see Supplementary Table 7 for exact p values).

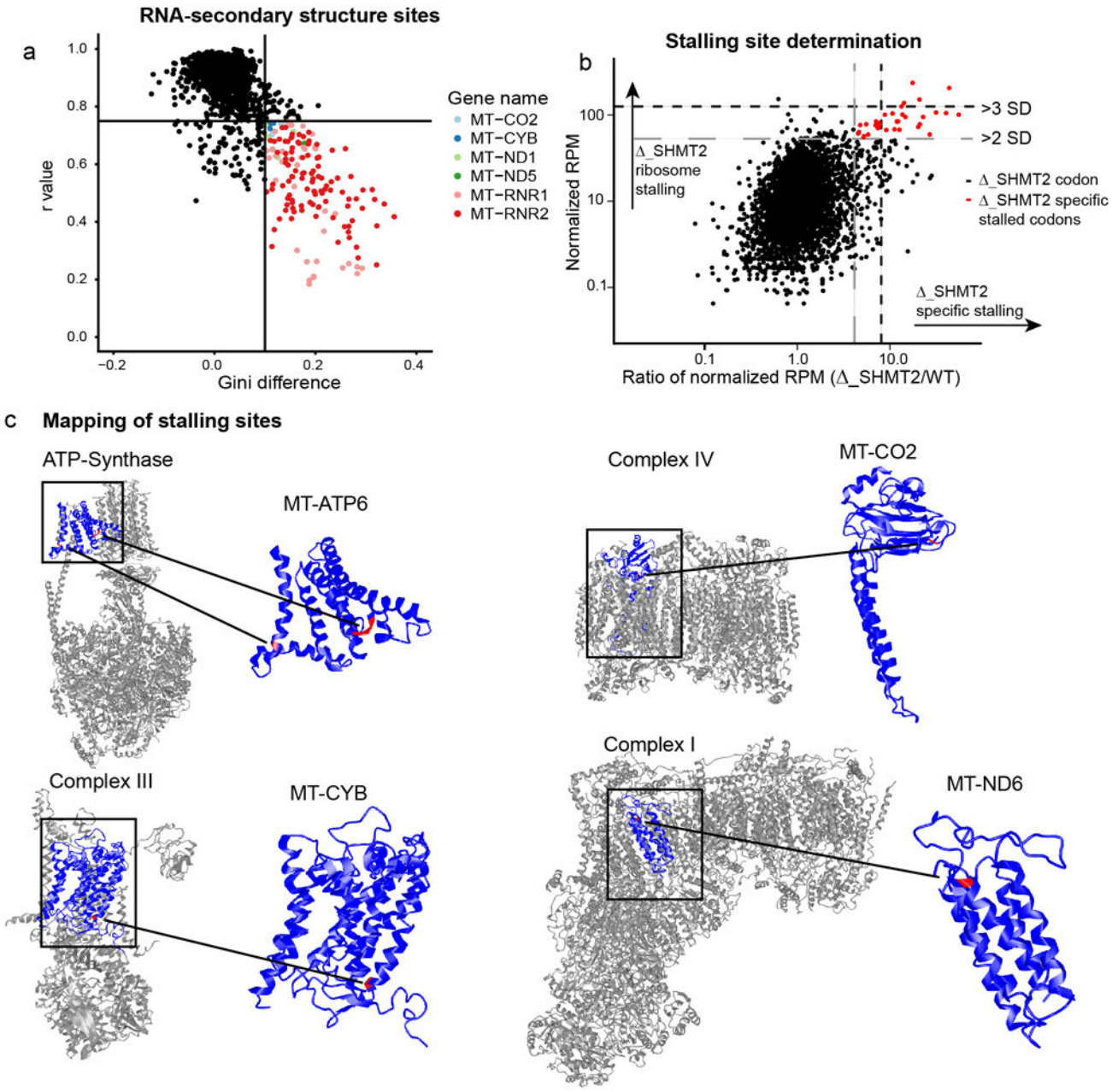

Extended Data Figure 8. Investigation of mRNA and protein secondary structure effects on mitochondrial ribosome stalling sites

a, Identification of mitochondrial RNA secondary structure based on analysis of the mitochondrial transcript data from the dimethyl sulphate sequencing dataset published by Rouskin S. et al. R-value and Gini difference were calculated to detect changes in nucleotide reactivity between the *in vivo* and denatured condition for the complete mitochondrial transcriptome. Colored points indicate structured regions given in Supplementary Table 4. **b**, Determination of ribosome stalling sites in HCT116 SHMT2 knockout cell lines. Data points represent individual codons of all 13 mitochondrial protein-coding transcripts. For each codon, the y-axis indicates the ribosome counts normalized to the gene-median in reads

per million (RPM). The x-axis indicates the ratio of normalized counts in SHMT2 knockout to normalized counts in wild-type HCT116. Two and three standard deviations (SD) above the mean of all codons in the genome are indicated by the grey and black dotted line respectively. Highlighted in red are codons > 2 SD. **c**, Mapping of AAG/UUG codons from SHMT2 knockout-specific ribosome stalling sites (> 3 SD) on protein structures. For **b** and **c**, analysis based on ribosome profiling data presented in main text Figure 3 with two technical replicates of two independent samples. A list of identified codons and mapped AAG/UUG sites is given in Supplementary Table 5.

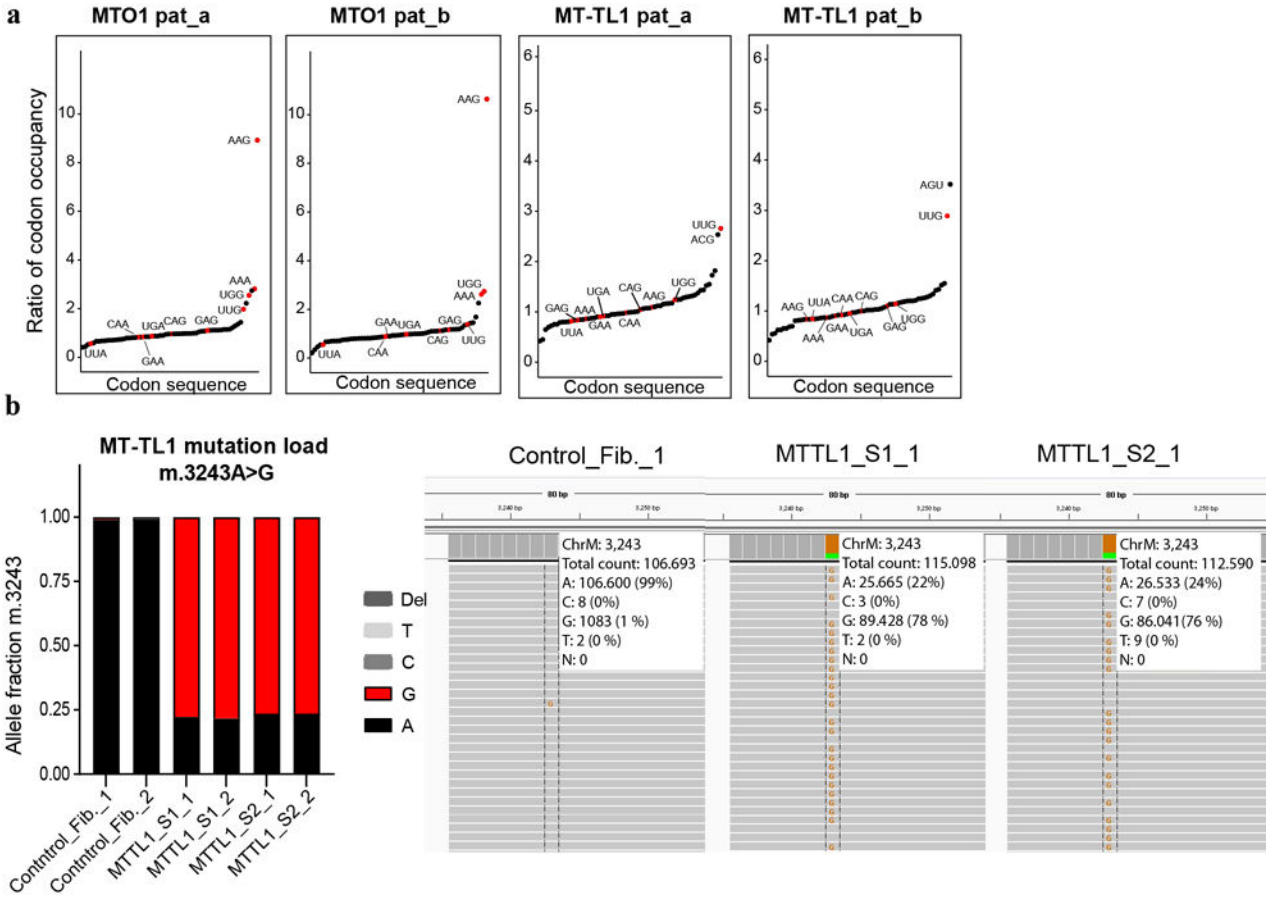

Extended Data Figure 9. Mitochondrial transcript codon occupancy from ribosome profiling of individual patient lines

a, Codon-specific mitochondrial ribosome occupancy ratio (patient/control fibroblasts) in individual patient derived cell lines (n = 1 for each individual patient, normalized to mean of n = 2 control fibroblast lines). Patients had either nuclear *MTO1* missense mutations (pat_a c.[1261-5T>G];[1430G>A], pat_b c.[1222T>A];[1222T>A]) or were diagnosed with MELAS and carry the recurrent point mutation m.3243A>G in the mitochondrial gene for tRNA Leu1 (*MT-TL1*). **b**, Next-generation sequencing of mtDNA mutation load m. 3243A>G (*MT-TL1)* in control fibroblasts and MELAS patient cell lines. Each bar shows one biological replicate for control and patient cell lines. Integrative genomics viewer sequencing raw data is shown on the right.

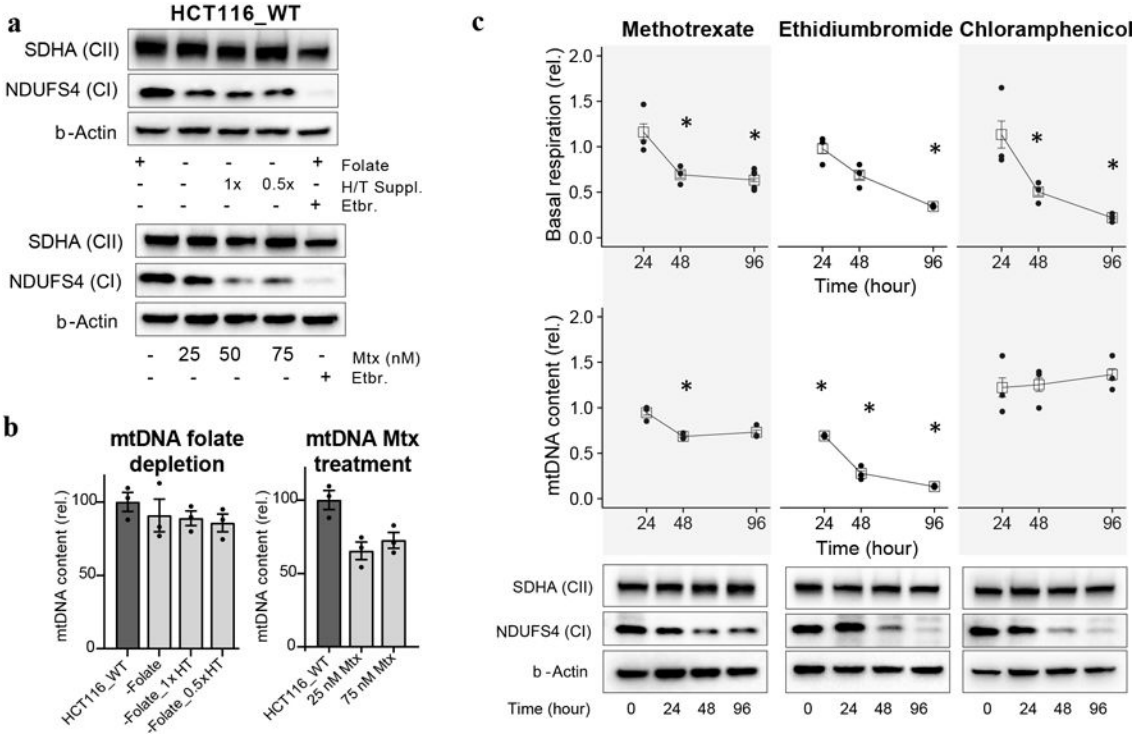

Extended Data Figure 10. Effects of targeting one-carbon metabolism on mitochondrial function

a, Mitochondrial complex I and II levels on immunoblot after growth in the absence of folate for 5 passages or in the presence of the indicated methotrexate concentration for 96 h. Ethidium bromide (250 nM) was used as a positive control. **b**, Cellular mtDNA levels in HCT116 cells upon folate depletion (with or without hypoxanthine and thymidine as rescue agents) or presence of methotrexate for 96 h ($n = 3$). **c**, In an effort to determine if the decrease in respiration due to methotrexate arises from methotrexate depleting mitochondrial DNA, impairing mitochondrial translation, or a combination, we compared the effects in HCT116 cells of methotrexate (50 nM) to ethidium bromide (250 nM = 100 ng/ml), which is classically used to deplete mitochondrial DNA, and to chloramphenicol (310 μM = 100 μg/ml), which blocks mitochondrial translation. After 48 h of treatment, methotrexate and ethidium bromide both decreased oxygen consumption and DNA content. Importantly, despite ethidium bromide much more strongly depleting mitochondrial DNA, methotrexate had an equivalent effect on oxygen consumption consistent with methotrexate's effect on oxygen consumption being in part via mitochondrial translation inhibition. Data is normalized and compared to untreated control (all $n = 3$; except oxygen consumption methotrexate 96 h $n = 6$ and control $n = 4$). Data are reported as mean ± s.e.m; n indicates the number of biological replicates. Significance is calculated by two-tailed Student´s t-test * $P < 0.01$ (see Supplementary Table 7 for exact p values), Abbreviations: H/T, hypoxanthine (100 μM)/thymidine (16 μM); Mtx., methotrexate.

Supplementary Material

Refer to Web version on PubMed Central for supplementary material.

Acknowledgments

We thank T. Pan at University of Chicago, W. Lu, L. Chen, and all other members of the Rabinowitz lab, Lance Parsons and Wei Wang from the Sequencing Core at Princeton, and Tharan Srikumar from the Proteomics Core facility at Princeton. This work was supported by funding to J.D.R. from the US National Institutes of Health (NIH) (R01CA163591 and DP1DK113653) and StandUp to Cancer (SU2C-AACR-DT-20-16). G.S.D. was supported by a postdoctoral fellowship (PF-15-190-01- TBE) from the American Cancer Society. J.A.M. was supported by the science fund of the Paracelsus Medical University Salzburg (E-12/15/076-MAY). Z.G. was supported by grants from the NIH (1R01GM107384 and 1DP1OD019133) and National Science Foundation (NSF) (CBET-1330288) and a Human Frontiers Young Investigator Award (RGY0076/2013).

J.D.R. is a founder of Raze Therapeutics, which aims to target 1C metabolism for cancer therapy.

References

1. Fox JT, Stover PJ. Folate-mediated one-carbon metabolism. Vitamins and hormones. 2008; 79:1–44. DOI: 10.1016/s0083-6729(08)00401-9 [PubMed: 18804690]
2. Tibbetts AS, Appling DR. Compartmentalization of Mammalian folate-mediated one-carbon metabolism. Annu Rev Nutr. 2010; 30:57–81. DOI: 10.1146/annurev.nutr.012809.104810 [PubMed: 20645850]
3. Ducker GS, Rabinowitz JD. One-Carbon Metabolism in Health and Disease. Cell metabolism. 2016
4. Lipsky PE, et al. Infliximab and methotrexate in the treatment of rheumatoid arthritis. Anti-Tumor Necrosis Factor Trial in Rheumatoid Arthritis with Concomitant Therapy Study Group. The New England journal of medicine. 2000; 343:1594–1602. DOI: 10.1056/nejm200011303432202 [PubMed: 11096166]
5. Chabner BA, Roberts TG Jr. Timeline: Chemotherapy and the war on cancer. Nature reviews Cancer. 2005; 5:65–72. DOI: 10.1038/nrc1529 [PubMed: 15630416]
6. Ron-Harel N, et al. Mitochondrial Biogenesis and Proteome Remodeling Promote One-Carbon Metabolism for T Cell Activation. Cell metabolism. 2016; 24:104–117. DOI: 10.1016/j.cmet.2016.06.007 [PubMed: 27411012]
7. Nilsson R, et al. Metabolic enzyme expression highlights a key role for MTHFD2 and the mitochondrial folate pathway in cancer. Nature communications. 2014; 5:3128.
8. Kim D, et al. SHMT2 drives glioma cell survival in ischaemia but imposes a dependence on glycine clearance. Nature. 2015; 520:363–367. DOI: 10.1038/nature14363 [PubMed: 25855294]
9. Ducker GS, et al. Reversal of Cytosolic One-Carbon Flux Compensates for Loss of the Mitochondrial Folate Pathway. Cell metabolism. 2016; 23:1140–1153. DOI: 10.1016/j.cmet.2016.04.016 [PubMed: 27211901]
10. Garrow TA, et al. Cloning of human cDNAs encoding mitochondrial and cytosolic serine hydroxymethyltransferases and chromosomal localization. The Journal of biological chemistry. 1993; 268:11910–11916. [PubMed: 8505317]
11. Gohil VM, et al. Nutrient-sensitized screening for drugs that shift energy metabolism from mitochondrial respiration to glycolysis. Nature biotechnology. 2010; 28:249–255. DOI: 10.1038/nbt.1606
12. Mullen AR, et al. Reductive carboxylation supports growth in tumour cells with defective mitochondria. Nature. 2011; 481:385–388. DOI: 10.1038/nature10642 [PubMed: 22101431]
13. Sullivan LB, et al. Supporting Aspartate Biosynthesis Is an Essential Function of Respiration in Proliferating Cells. Cell. 2015; 162:552–563. DOI: 10.1016/j.cell.2015.07.017 [PubMed: 26232225]
14. Birsoy K, et al. An Essential Role of the Mitochondrial Electron Transport Chain in Cell Proliferation Is to Enable Aspartate Synthesis. Cell. 2015; 162:540–551. DOI: 10.1016/j.cell.2015.07.016 [PubMed: 26232224]
15. Iborra FJ, Kimura H, Cook PR. The functional organization of mitochondrial genomes in human cells. BMC biology. 2004; 2:9. [PubMed: 15157274]
16. Brown SS, Neal GE, Williams DC. Subcellular distribution of some folic acid-linked enzymes in rat liver. Biochem J. 1965; 97:34c–36c.

17. Anderson DD, Quintero CM, Stover PJ. Identification of a de novo thymidylate biosynthesis pathway in mammalian mitochondria. Proceedings of the National Academy of Sciences of the United States of America. 2011; 108:15163–15168. DOI: 10.1073/pnas.1103623108 [PubMed: 21876188]
18. Kozak M. Comparison of initiation of protein synthesis in procaryotes, eucaryotes, and organelles. Microbiological reviews. 1983; 47:1–45. [PubMed: 6343825]
19. Tucker EJ, et al. Mutations in MTFMT underlie a human disorder of formylation causing impaired mitochondrial translation. Cell metabolism. 2011; 14:428–434. DOI: 10.1016/j.cmet.2011.07.010 [PubMed: 21907147]
20. Saada A, et al. Mutant mitochondrial thymidine kinase in mitochondrial DNA depletion myopathy. Nature genetics. 2001; 29:342–344. DOI: 10.1038/ng751 [PubMed: 11687801]
21. Calvo SE, Mootha VK. The mitochondrial proteome and human disease. Annu Rev Genomics Hum Genet. 2010; 11:25–44. DOI: 10.1146/annurev-genom-082509-141720 [PubMed: 20690818]
22. Agris PF, Vendeix FA, Graham WD. tRNA's wobble decoding of the genome: 40 years of modification. Journal of molecular biology. 2007; 366:1–13. DOI: 10.1016/j.jmb.2006.11.046 [PubMed: 17187822]
23. Van Haute L, et al. Deficient methylation and formylation of mt-tRNA(Met) wobble cytosine in a patient carrying mutations in NSUN3. Nature communications. 2016; 7:12039.
24. Putz J, Dupuis B, Sissler M, Florentz C. Mamit-tRNA, a database of mammalian mitochondrial tRNA primary and secondary structures. Rna. 2007; 13:1184–1190. DOI: 10.1261/rna.588407 [PubMed: 17585048]
25. Fu Y, et al. The AlkB domain of mammalian ABH8 catalyzes hydroxylation of 5-methoxycarbonylmethyluridine at the wobble position of tRNA. Angewandte Chemie (International ed in English). 2010; 49:8885–8888. DOI: 10.1002/anie.201001242 [PubMed: 20583019]
26. Songe-Moller L, et al. Mammalian ALKBH8 possesses tRNA methyltransferase activity required for the biogenesis of multiple wobble uridine modifications implicated in translational decoding. Mol Cell Biol. 2010; 30:1814–1827. DOI: 10.1128/mcb.01602-09 [PubMed: 20123966]
27. Yasukawa T, et al. Defect in modification at the anticodon wobble nucleotide of mitochondrial tRNA(Lys) with the MERRF encephalomyopathy pathogenic mutation. FEBS Lett. 2000; 467:175–178. [PubMed: 10675533]
28. Yasukawa T, Suzuki T, Ueda T, Ohta S, Watanabe K. Modification defect at anticodon wobble nucleotide of mitochondrial tRNAs(Leu)(UUR) with pathogenic mutations of mitochondrial myopathy, encephalopathy, lactic acidosis, and stroke-like episodes. The Journal of biological chemistry. 2000; 275:4251–4257. [PubMed: 10660592]
29. Suzuki T, Suzuki T. A complete landscape of post-transcriptional modifications in mammalian mitochondrial tRNAs. Nucleic acids research. 2014; 42:7346–7357. DOI: 10.1093/nar/gku390 [PubMed: 24831542]
30. Ghezzi D, et al. Mutations of the mitochondrial-tRNA modifier MTO1 cause hypertrophic cardiomyopathy and lactic acidosis. Am J Hum Genet. 2012; 90:1079–1087. DOI: 10.1016/j.ajhg.2012.04.011 [PubMed: 22608499]
31. Kopajtich R, et al. Mutations in GTPBP3 cause a mitochondrial translation defect associated with hypertrophic cardiomyopathy, lactic acidosis, and encephalopathy. Am J Hum Genet. 2014; 95:708–720. DOI: 10.1016/j.ajhg.2014.10.017 [PubMed: 25434004]
32. Moukadiri I, et al. Evolutionarily conserved proteins MnmE and GidA catalyze the formation of two methyluridine derivatives at tRNA wobble positions. Nucleic acids research. 2009; 37:7177–7193. DOI: 10.1093/nar/gkp762 [PubMed: 19767610]
33. Doherty EA, Batey RT, Masquida B, Doudna JA. A universal mode of helix packing in RNA. Nat Struct Biol. 2001; 8:339–343. DOI: 10.1038/86221 [PubMed: 11276255]
34. Rouskin S, Zubradt M, Washietl S, Kellis M, Weissman JS. Genome-wide probing of RNA structure reveals active unfolding of mRNA structures in vivo. Nature. 2014; 505:701–705. DOI: 10.1038/nature12894 [PubMed: 24336214]
35. Kirino Y, Goto Y, Campos Y, Arenas J, Suzuki T. Specific correlation between the wobble modification deficiency in mutant tRNAs and the clinical features of a human mitochondrial

disease. Proceedings of the National Academy of Sciences of the United States of America. 2005; 102:7127–7132. DOI: 10.1073/pnas.0500563102 [PubMed: 15870203]

36. Grim J, Chladek J, Martinkova J. Pharmacokinetics and pharmacodynamics of methotrexate in non-neoplastic diseases. Clinical pharmacokinetics. 2003; 42:139–151. DOI: 10.2165/00003088-200342020-00003 [PubMed: 12537514]
37. Mayr JA, et al. Spectrum of combined respiratory chain defects. J Inherit Metab Dis. 2015; 38:629–640. DOI: 10.1007/s10545-015-9831-y [PubMed: 25778941]
38. Ran FA, et al. Genome engineering using the CRISPR-Cas9 system. Nature protocols. 2013; 8:2281–2308. DOI: 10.1038/nprot.2013.143 [PubMed: 24157548]
39. Szebenyi DM, Musayev FN, di Salvo ML, Safo MK, Schirch V. Serine hydroxymethyltransferase: role of glu75 and evidence that serine is cleaved by a retroaldol mechanism. Biochemistry. 2004; 43:6865–6876. DOI: 10.1021/bi049791y [PubMed: 15170323]
40. Contestabile R, et al. Role of tyrosine 65 in the mechanism of serine hydroxymethyltransferase. Biochemistry. 2000; 39:7492–7500. [PubMed: 10858298]
41. Iurescia S, Condo I, Angelaccio S, Delle Fratte S, Bossa F. Site-directed mutagenesis techniques in the study of Escherichia coli serine hydroxymethyltransferase. Protein expression and purification. 1996; 7:323–328. [PubMed: 8860659]
42. Tischner C, et al. MTO1 mediates tissue specificity of OXPHOS defects via tRNA modification and translation optimization, which can be bypassed by dietary intervention. Hum Mol Genet. 2015; 24:2247–2266. DOI: 10.1093/hmg/ddu743 [PubMed: 25552653]
43. Sasarman F, Shoubridge EA. Radioactive labeling of mitochondrial translation products in cultured cells. Methods in molecular biology (Clifton, NJ). 2012; 837:207–217. DOI: 10.1007/978-1-61779-504-6_14
44. Clasquin, MF., Melamud, E., Rabinowitz, JD. LC-MS data processing with MAVEN: a metabolomic analysis and visualization engine. In: Baxevanis, Andreas D., et al., editors. Current protocols in bioinformatics. 2012. Chapter 14, Unit14.11
45. Afgan E, et al. The Galaxy platform for accessible, reproducible and collaborative biomedical analyses: 2016 update. Nucleic acids research. 2016; 44:W3–w10. DOI: 10.1093/nar/gkw343 [PubMed: 27137889]
46. R_Core_Team. R: A language and environment for statistical computing. R Foundation for Statistical Computing; Vienna, Austria: 2016. URL https://www.R-project.org/
47. Marcel M. Cutadapt removes adapter sequences from high-throughput sequencing reads. EMBnet journal. 2011; 17 http://dx.doi.org/10.14806/ej.17.1.200.
48. Kim D, et al. TopHat2: accurate alignment of transcriptomes in the presence of insertions, deletions and gene fusions. Genome biology. 2013; 14:R36. [PubMed: 23618408]
49. Anders S, Pyl PT, Huber W. HTSeq–a Python framework to work with high-throughput sequencing data. Bioinformatics (Oxford, England). 2015; 31:166–169. DOI: 10.1093/bioinformatics/btu638
50. Love MI, Huber W, Anders S. Moderated estimation of fold change and dispersion for RNA-seq data with DESeq2. Genome biology. 2014; 15:550. [PubMed: 25516281]
51. Bao XR, et al. Mitochondrial dysfunction remodels one-carbon metabolism in human cells. eLife. 2016; 5
52. Mayr JA, et al. Mitochondrial phosphate-carrier deficiency: a novel disorder of oxidative phosphorylation. Am J Hum Genet. 2007; 80:478–484. DOI: 10.1086/511788 [PubMed: 17273968]
53. Langmead B, Salzberg SL. Fast gapped-read alignment with Bowtie 2. Nat Methods. 2012; 9:357–359. DOI: 10.1038/nmeth.1923 [PubMed: 22388286]
54. Ramirez F, et al. deepTools2: a next generation web server for deep-sequencing data analysis. Nucleic acids research. 2016; 44:W160–165. DOI: 10.1093/nar/gkw257 [PubMed: 27079975]
55. Garrison E, Marth G. Haplotype-based variant detection from short-read sequencing. ArXiv e-prints. 2012; 1207 <http://adsabs.harvard.edu/abs/2012arXiv1207.3907G>.
56. Hahne F, Ivanek R. Visualizing Genomic Data Using Gviz and Bioconductor. Methods in molecular biology (Clifton, NJ). 2016; 1418:335–351. DOI: 10.1007/978-1-4939-3578-9_16

57. Ingolia NT, Brar GA, Rouskin S, McGeachy AM, Weissman JS. The ribosome profiling strategy for monitoring translation in vivo by deep sequencing of ribosome-protected mRNA fragments. Nature protocols. 2012; 7:1534–1550. DOI: 10.1038/nprot.2012.086 [PubMed: 22836135]
58. Rooijers K, Loayza-Puch F, Nijtmans LG, Agami R. Ribosome profiling reveals features of normal and disease-associated mitochondrial translation. Nature communications. 2013; 4:2886.
59. Couvillion, MT., Soto, IC., Shipkovenska, G., Churchman, LS. Synchronized mitochondrial and cytosolic translation programs. Nature. 2016. advance online publicationhttp://www.nature.com/nature/journal/vaop/ncurrent/abs/nature18015.html#supplementary-information
60. Dunn, JG. plastid: a positional library for sequencing analysis. 2016. <http://plastid.readthedocs.io.>
61. Nakahigashi K, et al. Effect of codon adaptation on codon-level and gene-level translation efficiency in vivo. BMC genomics. 2014; 15:1115. [PubMed: 25512115]
62. Balakrishnan R, Oman K, Shoji S, Bundschuh R, Fredrick K. The conserved GTPase LepA contributes mainly to translation initiation in Escherichia coli. Nucleic acids research. 2014; 42:13370–13383. DOI: 10.1093/nar/gku1098 [PubMed: 25378333]
63. Oh E, et al. Selective ribosome profiling reveals the cotranslational chaperone action of trigger factor in vivo. Cell. 2011; 147:1295–1308. DOI: 10.1016/j.cell.2011.10.044 [PubMed: 22153074]
64. Dunn JG, Foo CK, Belletier NG, Gavis ER, Weissman JS. Ribosome profiling reveals pervasive and regulated stop codon readthrough in Drosophila melanogaster. eLife. 2013; 2:e01179. [PubMed: 24302569]
65. Wang Y, Geer LY, Chappey C, Kans JA, Bryant SH. Cn3D: sequence and structure views for Entrez. Trends in biochemical sciences. 2000; 25:300–302. [PubMed: 10838572]
66. Krogh A, Larsson B, von Heijne G, Sonnhammer EL. Predicting transmembrane protein topology with a hidden Markov model: application to complete genomes. Journal of molecular biology. 2001; 305:567–580. DOI: 10.1006/jmbi.2000.4315 [PubMed: 11152613]
67. Del Campo C, Bartholomaus A, Fedyunin I, Ignatova Z. Secondary Structure across the Bacterial Transcriptome Reveals Versatile Roles in mRNA Regulation and Function. PLoS Genet. 2015; 11:e1005613. [PubMed: 26495981]
68. Srere PA. Citrate synthase. Methods in enzymology. 1969; 13:3–5.
69. Feichtinger RG, et al. Low aerobic mitochondrial energy metabolism in poorly- or undifferentiated neuroblastoma. BMC cancer. 2010; 10:149. [PubMed: 20398431]
70. Rustin P, et al. Biochemical and molecular investigations in respiratory chain deficiencies. Clinica chimica acta; international journal of clinical chemistry. 1994; 228:35–51. [PubMed: 7955428]
71. Clayton DA, Shadel GS. Isolation of mitochondria from tissue culture cells. Cold Spring Harb Protoc. 2014; 2014 pdb prot080002.
72. Zheng G, et al. ALKBH5 is a mammalian RNA demethylase that impacts RNA metabolism and mouse fertility. Molecular cell. 2013; 49:18–29. DOI: 10.1016/j.molcel.2012.10.015 [PubMed: 23177736]
73. Ogata T, et al. Chemical synthesis and properties of 5-taurinomethyluridine and 5-taurinomethyl-2-thiouridine. The Journal of organic chemistry. 2009; 74:2585–2588. DOI: 10.1021/jo802697r [PubMed: 19219973]
74. Shevchenko A, Tomas H, Havlis J, Olsen JV, Mann M. In-gel digestion for mass spectrometric characterization of proteins and proteomes. Nat Protoc. 2006; 1:2856–2860. DOI: 10.1038/nprot.2006.468 [PubMed: 17406544]
75. Dorfer V, et al. MS Amanda, a universal identification algorithm optimized for high accuracy tandem mass spectra. Journal of proteome research. 2014; 13:3679–3684. DOI: 10.1021/pr500202e [PubMed: 24909410]
76. Eng JK, McCormack AL, Yates JR. An approach to correlate tandem mass spectral data of peptides with amino acid sequences in a protein database. J Am Soc Mass Spectrom. 1994; 5:976–989. DOI: 10.1016/1044-0305(94)80016-2 [PubMed: 24226387]
77. Bern M, Kil YJ, Becker C. Byonic: advanced peptide and protein identification software. Curr Protoc Bioinformatics. 2012 Chapter 13, Unit13 20,

78. Spivak M, Weston J, Bottou L, Kall L, Noble WS. Improvements to the percolator algorithm for Peptide identification from shotgun proteomics data sets. Journal of proteome research. 2009; 8:3737–3745. DOI: 10.1021/pr801109k [PubMed: 19385687]

79. MacLean B, et al. Skyline: an open source document editor for creating and analyzing targeted proteomics experiments. Bioinformatics (Oxford, England). 2010; 26:966–968. DOI: 10.1093/bioinformatics/btq054

80. Schilling B, et al. Platform-independent and label-free quantitation of proteomic data using MS1 extracted ion chromatograms in skyline: application to protein acetylation and phosphorylation. Mol Cell Proteomics. 2012; 11:202–214. DOI: 10.1074/mcp.M112.017707 [PubMed: 22454539]

81. Renwick SB, Snell K, Baumann U. The crystal structure of human cytosolic serine hydroxymethyltransferase: a target for cancer chemotherapy. Structure. 1998; 6:1105–1116. [PubMed: 9753690]

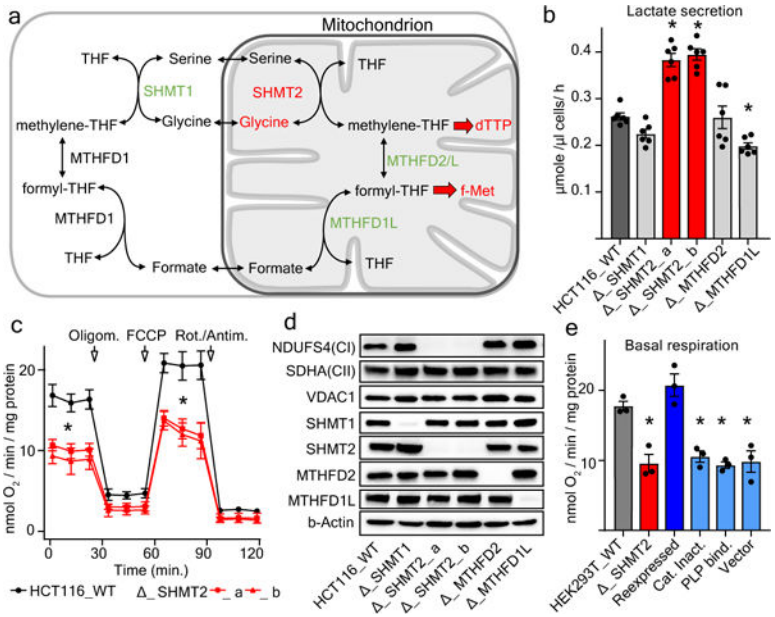

Figure 1. Mitochondrial respiratory chain function is dependent on SHMT2 catalytic activity

a, 1C pathway and known mitochondrial products. **b**, Lactate secretion of HCT116 knockout cell lines ($n = 6$). **c**, Oxygen consumption rate measured by Seahorse XF analyzer ($n = 3$). **d**, Immunoblot for mitochondrial respiratory complex I and II proteins (NDUFS4 and SDHA), 1C enzymes, and mitochondrial mass (VDAC1). **e**, Basal respiration ($n = 3$) upon re-expression of wild-type or catalytically deficient mutant forms of SHMT2 in HEK293T knockout cell lines. Results are given as mean ± s.e.m; n indicates the number of biological replicates, which for Seahorse experiments refers to independent plates on separate days. Significance is calculated by two-tailed Student´s t-test. * $P < 0.01$ (see Supplementary Table 7 for exact p values). Abbreviations: methylene-THF, 5,10-methylene-THF; formyl-THF, 10-formyl-THF; THF, tetrahydrofolate; dTTP, deoxythymidine triphosphate; f-Met, n-formyl-methionine; Oligom., oligomycin; Rot./Antim., rotenone/antimycin; Cat. inact., catalytically inactive SHMT2; PLP bind., PLP binding-deficient SHMT2.

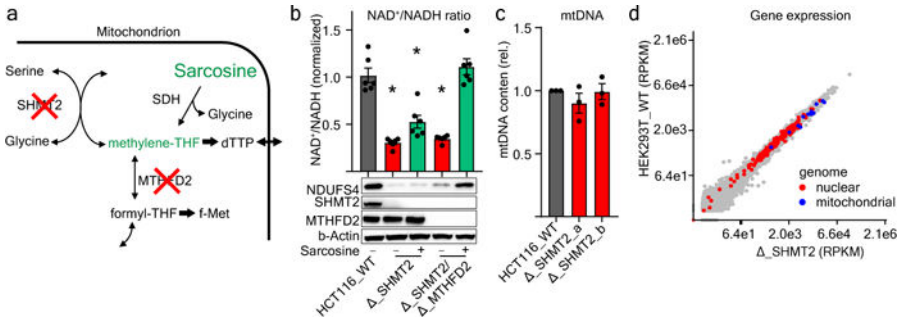

Figure 2. ΔSHMT2 induced respiratory chain deficiency is caused by mitochondrial 5,10-methylene-THF depletion but is unrelated to dTTP synthesis

a, Sarcosine serves as a SHMT2-independent source of mitochondrial methylene-THF. **b**, NAD^+/NADH ratio ($n = 6$) and NDUFS4 (complex I) protein expression upon sarcosine supplementation (1 mM) in SHMT2 single and SHMT2/MTHFD2 double knockout cell lines compared to wild-type. **c** and **d**, Functional readouts for mitochondrial dTTP status based on **c**, mtDNA level ($n = 3$) determined by quantitative real-time PCR and **d**, gene expression in SHMT2 knockout and wild-type HEK293T cells. For **d**, each data point represents mean gene expression of two biological replicates of two independent knockout clones ($n = 4$) and two wild-type replicates ($n = 2$). Genes linked to OXPHOS function[37] are highlighted in red (nuclear encoded) or blue (mitochondrial encoded). Significantly differentially-expressed genes are listed in Supplementary Table 2. Bar graphs show mean ± s.e.m; n indicates the number of independent biological replicates. Significance is calculated by two-tailed Student´s t-test. * $P < 0.01$ (see Supplementary Table 7 for exact p values). Abbreviations: dTTP, deoxythymidine triphosphate; mtDNA, mitochondrial DNA; RPKM, reads per kilobase per million mapped reads.

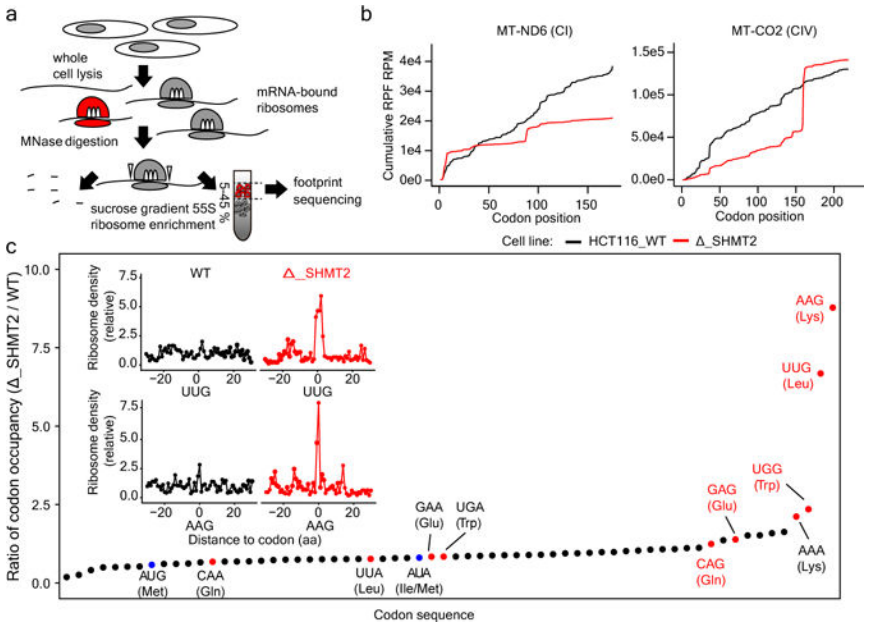

Figure 3. Mitochondrial ribosome profiling reveals ΔSHMT2 cells are deficient in translating specific guanosine-ending codons

a, Workflow of mitochondrial ribosome profiling: translation was halted using chloramphenicol and immersion into liquid nitrogen, cells were lysed and RNA was digested using Micrococcal nuclease (MNase). Following sucrose-gradient enrichment for mitochondrial ribosomes (shaded in red), protected fragments were sequenced. **b**, Mean cumulative ribosome density along selected mitochondrial transcripts. Black is wild-type HCT116 and red is ΔSHMT2. Additional transcripts are given in Extended Data Fig. 6a. **c**, Mean codon-specific mitochondrial ribosome occupancy ($HCT116_{\Delta SHMT2}/HCT116_{wt}$;). Data points highlighted in red correspond to codons that are decoded by tRNAs carrying the 5-taurinomethyluridine modification. Text labels highlighted in red correspond to the subset of those codons that end in guanosine and thus require wobble-base pairing. Methionine codons are highlighted in blue and show no increased codon occupancy. The insert shows mean normalized ribosome density relative to UUG and AAG codon position. **b** and **c**, two technical replicates of two independent samples. Abbreviations: RPF, ribosome protected fragment; RPM, reads per million mapped reads.

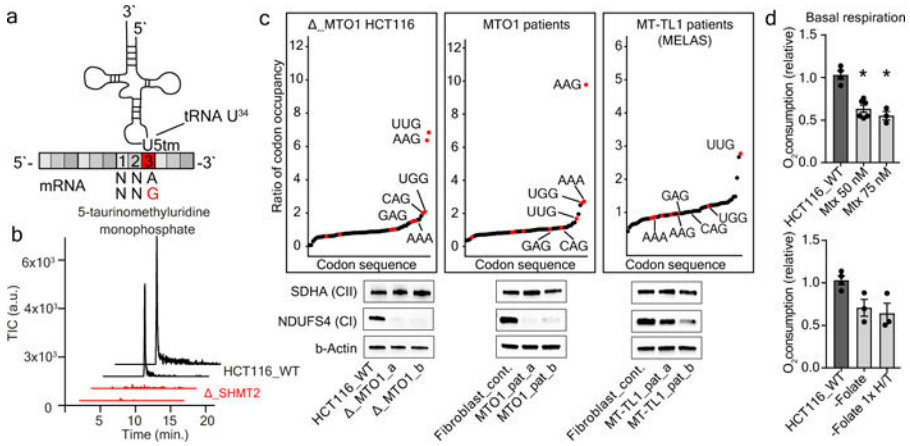

Figure 4. MTO1/GTPBP3 dependent tRNA methylation requires mitochondrial 5,10-methylene-THF

a, Interaction of tRNA position 34 anticodon loop modified base with messenger RNA codon three position A/G, forming a non-Watson-Crick base pair. **b**, Total ion chromatogram of 5-taurinomethyluridine monophosphate (m/z = 460.043) from digested mitochondrial tRNAs. 5-formylcytidine monophosphate was not altered (Extended Data Fig. 7a). **c**, Mean codon-specific mitochondrial ribosome occupancy for HCT116 MTO1 knockout cell lines and primary patient derived fibroblasts carrying *MTO1* mutations or the *MT-TL1* m. 3243A>G MELAS variant ($n = 2$). Corresponding immunoblots are shown below. Individual patient data are in Extended Data Fig. 9a. **d**, Basal respiration rates measured using the Seahorse XF analyzer. Data were collected after growth in the absence of folate for 5 passages or in the presence of the indicated methotrexate concentration for 96 h ($n = 3$, except HCT116_WT $n = 4$ and Mtx 50 nM $n = 6$). Graphs show mean ± s.e.m; n indicates the number of biological replicates. Significance is calculated by two-tailed Student´s t-test. * $P < 0.01$ (see Supplementary Table 7 for exact p values). Abbreviations: Mtx, methotrexate; H/T, hypoxanthine (100 μM)/thymidine (16 μM).